Wave Induced Dynamics of Offshore Heavy Lift Cranes on Jack-Ups

Analysis of the annual probability of failure of the crane in normal operation

Loïc Appert

Technische Universiteit Delft

TU Delft

Wave Induced Dynamics of Offshore Heavy Lift Cranes on Jack-Ups

Analysis of the annual probability of failure of the crane in normal operation

by

Loïc Appert

to obtain the degree of Master of Science
in Offshore & Dredging Engineering
at the Delft University of Technology,
to be defended publicly on Thursday June 22, 2023 at 14:00 PM

Student number:	4582276	
Project duration:	May 17, 2022 – June 22, 2023	
Thesis committee:	Dr. E. Lourens,	TU Delft, Chair
	Ir. J. S. Hoving,	TU Delft, supervisor
	Ir. T. J. P. Blankenstein,	GustoMSC, daily supervisor
	Ir. P. van Uchelen,	GustoMSC, supervisor

This thesis is confidential and cannot be made public until June 22, 2025.

TU Delft GustoMSC | NOV

Preface

Dear reader,

This report has been written in the context of my thesis, to conclude my master Offshore & Dredging Engineering at the Delft University of Technology (TU Delft). This thesis has been performed on wave induced dynamics of offshore heavy lift cranes on jack-ups, which hopefully contributes in the transition to a more sustainable future.

During this research, I received the support and guidance from several people. To start, I would like to thank my TU Delft supervisor, Eliz-Mari Lourens, who gave me valuable support and feedback during the thesis. Next, I would like to thank Jeroen Hoving for his insightful feedback during the various progress meetings.

This thesis has been performed under the guidance of GustoMSC. From GustoMSC, I would like to thank Tobias Blankenstein, for his time and enthusiasm. Your support and numerous feedback were very helpful. I would like to thank Perry van Uchelen, for his critical eye and feedback. Additionally, I would like to thank all other employees of GustoMSC which shared their knowledge and supported me during the duration of my thesis.

At last, I would like to thank my family and friends for their support throughout my study and this thesis.

Loïc Appert
Delft, June 2023

Abstract

Due to the increasing size of offshore wind turbines, the jack-up vessels and cranes installing them need to increase in size. The increase in length of the crane boom results in an increase of the dynamic response of the crane. This increase in response results in higher loads in the crane. The magnitude of the higher loads are unknown and not yet accounted for in crane design. To get a better insight in the dynamic response of the crane and higher loads, a probabilistic model is developed to quantify the annual probability of the crane.

To define the different crane operations, a measurement data set of crane operations is made available. From this data set, the different lifts types, exposure times and occurrences are identified. Multiple jack-up configurations are chosen with different water depth and wave heading. Next to the crane and jack-up configuration, long-term wave statistics are used for the environmental conditions, as input for the probabilistic model.

Time-domain simulations are performed in a rigid multi-body analysis software, to simulate the dynamic response of the crane, due to wave induced excitations. Due to the random nature of waves, convergence of the results is researched. For this, numerous time-domain simulations with different sea-states have to be performed, this is unwanted.

A methodology is developed, using the frequency domain, to limit the number of required time-domain simulations. Using the devised methodology, configurations with similar statistical description can be identified and grouped.

The annual probability of failure can be calculated using the devised methodology and probabilistic model. The resulting annual probability of failure is small, much smaller than required. A sensitivity analysis is performed, it is found that the annual probability of failure depends greatly on the input of the probabilistic model.

From the results and sensitivity analysis, multiple recommendations are given to decrease the sensitivity of the result. It can be said that from the devised methodology, a basis has been laid to quantify the annual probability of failure of the crane in normal operations.

Contents

List of Figures

List of Tables

1

Introduction

With the increasing demand for renewable energy sources in the world, to decrease the dependency on fossil fuels and the aim to decrease polluting emissions. The offshore wind energy market is rapidly growing. GustoMSC, a NOV company, is a major player in the offshore wind installation market. They design jack-ups and their onboard cranes for the installation of offshore wind turbines. Over the past years, jack-ups and cranes, designed by GustoMSC, are rapidly increasing in size. This is due to the increasing size of installed wind turbines. In figure 1.1, it is shown that the installed capacity increased from 3 MW in 2010 to over 12 MW in 2021. This increase in capacity results in an increase in size of the wind turbine. The reason that turbines increase in size is that bigger turbines are deemed more cost-effective compared to smaller ones. It is expected that this trend will continue in the future and that in 2030 turbines with a capacity of 20 MW could be seen. This growth in size means that the installation vessels need to increase in size to be able to install these future wind turbines. The bigger wind turbines require longer cranes which can lift more to be able to install these future offshore wind turbines. Currently, at GustoMSC, cranes with booms of length's up to 130 meters are being commissioned and the next generation is expected to be at least 40 meters longer.

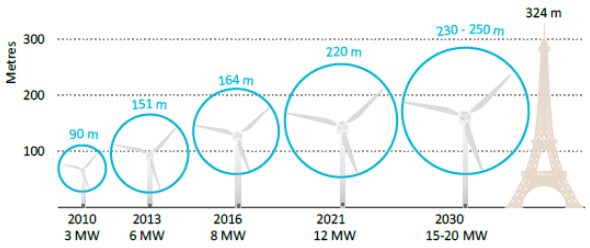

Figure 1.1: Increasing size of offshore wind turbines and expected future growth, IEA 2019 [10]

Additionally, offshore wind park locations are moving to deeper water with harsher environmental conditions. This is caused by the fact that available offshore sites in shallow water depth are getting scarce, as these sites were the first ones to be developed. The increase in depth requires longer legs for the jack-ups resulting in higher environmental loads. These higher loads will result in an increase in the dynamics response of the jack-up. This has an impact on the operability of the crane, as these motions will affect the crane dynamic response.

In the offshore wind turbine installation industry, the jack-ups currently in operation and the ones being built all have the same design philosophy. The jack-ups have four legs and make use of a leg encircling crane to lift the wind turbine components off its deck. It is also possible to transport and install the monopiles used as foundation of the wind turbine with these vessels. However, this thesis focusses on the installation of wind turbines and not the monopiles.

Previous research considering modelling of dynamic response of wind turbine blade installation has been performed, by Zhao [29] and Verma [27], taking into account the jack-up and crane dynamic response. Furthermore, extensive research has been performed on jack-up rigs for the offshore oil and

gas industry, most of these have been about the jack-up response due to waves. Two different conditions were investigated in these researches, survival and operational conditions. For this research, only operational conditions are considered, as no lifting operation will occur in survival conditions.

At GustoMSC, research has been done on the dynamic response of jack-ups due to earthquakes, by Linthorst [13], Blankenstein [3] and Engelen [6]. Engelen [6], investigated if it is required to model the crane as a substructure of the jack-up to account for the dynamic response of the jack-up due to the crane motions.

1.1. Problem definition

As mentioned above, the increasing water depth in which wind turbines are installed and the increasing size of the to be installed wind turbines, result in the increasing size of the jack-ups and the size of the onboard crane. The length of the crane boom needs to increase, which has an influence on the stiffness of the boom, see equation (1.1).

$$k = \frac{3 \cdot E \cdot I}{l^3} \tag{1.1}$$

In equation (1.1), k is the stiffness, E is the modulus of elasticity, I is the moment of inertia of the crane and l is the length of the boom. This change in stiffness has an influence on the natural period of the crane:

$$T_{nat} = 2 \cdot \pi \cdot \sqrt{\frac{k}{m}} \tag{1.2}$$

In equation (1.2), T_{nat} is the fundamental natural period and m the mass of the crane. Current state-of-the-art cranes have a boom length of 130 meters. For future jack-ups, crane booms with a length of 170 meters are envisaged. This means an increase in crane boom length by a factor of 1.3. In equation (1.1), the length of the boom is to the power of three, which means that the boom stiffness will reduce by a factor of 2.2. As the fundamental natural period is dependent on the stiffness, see equation (1.2), the fundamental natural period will increase. To counter this, the stiffness of the cranes needs to increase, which means that the mass needs to increase. This is unwanted, as this means that the maximum lifting capacity of the crane will decrease. The increase of the fundamental natural period induces an increase in the dynamic sensitivity at higher periods of the jack-up and the crane. In figure 1.2, the spectra of the crane, jack-up and JONSWAP are shown. The fundamental natural period of the crane moves towards the fundamental natural period of the jack-up. The jack-up fundamental natural period moves towards external excitations' period. These external excitations are, the wave loads. The sling spectrum is not shown as it is dependent on the sling length, but it can move towards the JONSWAP spectrum and result in resonance of the sling. Because the fundamental natural periods of the crane and jack-up move towards each other and towards the JONSWAP spectrum, the dynamic response increases.

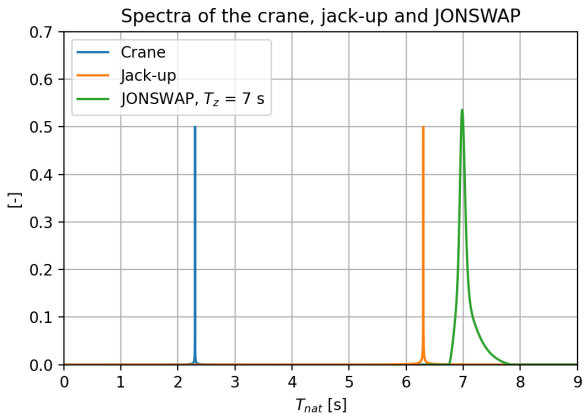

Figure 1.2: Example spectra of the crane, jack-up peak and a JONSWAP spectrum

GustoMSC is trying to develop a more profound understanding of these dynamics and the influence they have on the structural integrity of the crane. The same influence will apply to the increasing size

of the legs, that enable installation in deeper water. In these deeper waters, the environmental loads on the legs will increase, which adds-up to the increase in dynamic response of the jack-up and the crane.

Currently, for the design of cranes, DNV Lifting Appliances [26], only requires a static load case for the maximum load. To account for the loads due to the dynamic response of the crane caused by the wave induced excitations, a new load case needs to be considered.

This results in the following problem statement:

"Due to the increasing size of jack-ups and their crane, the wave induced excitations are expected to increase the dynamic response of the crane. The magnitude of the resulting higher loads are unknown and not yet accounted for in crane design. To get a better insight in the dynamic response of the crane and the higher loads, a probabilistic model is required to quantify the annual probability of failure of the crane."

1.2. Research question

From the problem statement described in section 1.1, the following research question is drawn. This research question is divided into multiple sub-questions:
What is the annual probability of failure (APF) of the crane, considering the relevant loads, crane operations and the crane resistance?

1. Which external loads need to be accounted for the dynamic response of the crane?
2. Which jack-up and crane configurations need to be accounted for, to mimic the operational profile of a jack-up installing wind turbines?
3. Are the present assumptions in the NX-motion crane model, correct?
4. Based on a spectral analysis of the different jack-up and crane configurations, is it possible to limit the required number of time-domain simulations?
5. Is it possible to calculate the expected maximum moment based on a spectral analysis?
6. What is the annual probability of failure (APF) of the crane, considering the relevant loads, crane operations and the crane resistance?
7. How is the APF influenced by different assumptions and input?

1.3. Report outline

To be able to answer the research questions stated above, first a literature research is done about jack-ups and cranes used for the installation of offshore wind turbines. The literature research about jack-up can be found in chapter 2 In chapter 3, the literature research about offshore heavy lifting cranes can be found. In chapter 4, the input used for the jack-up and crane model will be described. The environmental input and the measured data used to define the operational profile of the crane for installation of offshore wind turbines are shown. In chapter 5, the jack-up and crane model used for the time-domain simulations are explained. Furthermore, the maximum crane capacity is defined. In chapter 6, the methodology of the research will be explained. All the different steps to answer the research question are described. In chapter 7, after the model description and all the inputs are available, the results can be obtained using the described methodology. The results will be shown and discussed. A sensitivity analysis is performed to understand the impact of the assumptions. Finally, in chapter 8, a conclusion will be drawn from the results. Furthermore, the results will be discussed and recommendations for future research will be given.

2

Jack-up vessels used for offshore wind turbine installation

In this chapter, an introduction is given about jack-up vessels for offshore wind turbine installation. First, general information is given about jack-ups and the dimensions of the chosen jack-up for this research. The different external loads and dynamics on the jack-up will be reviewed. This comprises the environmental loads on the jack-up, which are divided into two parts, the hydrodynamic and the wind loads. The modelling of the soil-leg and leg-hull interaction will be discussed and at last the coupling between the jack-up motions and crane motions will be covered. Below, the different points that will be discussed are listed:

1. Introduction to jack-ups
2. Hydrodynamics load on jack-ups
3. Wind load on jack-ups
4. Hydrodynamics and wind load interaction
5. Soil-leg interaction
6. Leg-Hull connection effects
7. jack-up Crane coupling

2.1. Introduction to jack-ups

A typical jack-up for offshore wind turbine installation consists of a hull, on which the different wind turbine components are stowed. Four legs are used to lift the jack-up hull out of the water, each leg is connected to the hull through a jacking-house, see figure 2.1. In the jacking-house, pinions are present that are used to lift the hull to the wanted height above the water. At last, there is a leg encircling crane which is used to lift the wind turbine components. This crane is constructed around a leg to maximize deck space.

Figure 2.1: A typical jack-up used for the installation of offshore wind turbines, [18]

For this research, a NG-20000X jack-up vessel is chosen, which is designed by GustoMSC. This vessel is capable of transporting and installing four, 20 MW wind turbines, per trip. In table 2.1, the dimensions of the chosen jack-up vessel are listed.

Table 2.1: Dimension of chosen jack-up

Main parameter	**Value**
Hull length [m]	152
Hull width [m]	58
Hull depth [m]	12
Water depth [m]	70
Variable load [ton]	16500
Deck area [m^2]	5600
Deck load [ton / m^2]	10
Legs	
Leg type	Triangular open truss, X-braced
Leg length [m]	120
Leg length max. under hull [m]	90
Jacking system	
Type	Rack and Pinion with Variable Speed Drive
Pre-load [ton / leg]	20000
Jacking moves [/ year]	150 / year

2.2. Hydrodynamic load on the jack-ups

One of the main excitation mechanisms of a jack-up is the hydrodynamic load on the jack-up legs. Therefore, it is of importance to incorporate this in the model. The hydrodynamic load on the legs of a jack-up in elevated condition consists of two components; the wave load and the current load.

2.2.1. Wave load on the jack-ups legs

The wave induced dynamic response of the jack-up is the most important excitation mechanism used for the to be built probabilistic model. The wave load on the legs of the jack-up consists of a drag and inertia component. According to Tian et al. [20], the incident angle of the current and wave load have different influences on the inertia and drag component. The drag coefficient changes with the incident angle, on the other hand, the inertia coefficient remains almost the same. It is of importance to account for the incidence angle for the calculation of the hydrodynamic load on the jack-up legs.

The jack-up legs consist of slender tubular X-bracing, for this the Morison equation can be used to

approximate the wave force on the legs. The legs can be divided in strips where the surface of the slender tubular X-bracing can be calculated, for which the resulting wave force can be calculated. The total load is then found by integrating the force in each strip from the sea bed to the instantaneous sea surface level. In figure 2.2, the wave load dependence on the wave height can be seen. It can be remarked that depending on the wave height at each leg, the total load varies. To consider the changing wave height, Wheeler stretching needs to be added.

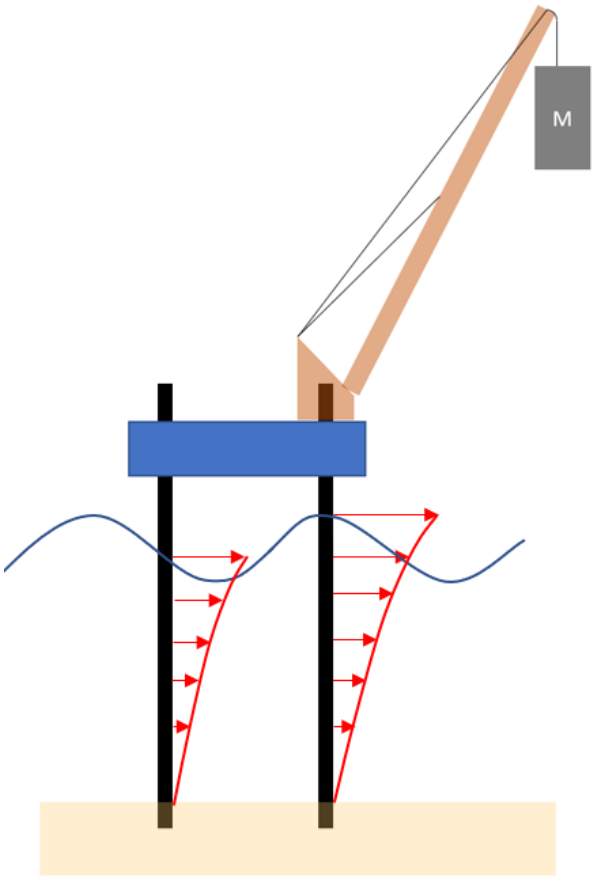

Figure 2.2: Wave load distribution, in red, on jack-up legs

Below, the Morison equation is shown:

$$f(z) = f_d(z) + f_i(z) = \frac{1}{2} \cdot \rho \cdot C_D \cdot D \cdot u(z) \cdot |u(z)| + \frac{\pi}{4} \cdot \rho \cdot C_M \cdot D^2 \cdot \dot{u}(z) \tag{2.1}$$

Where:

ρ	=	Water density
C_D	=	Drag coefficient
C_M	=	Inertia coefficient
D	=	Diameter of tubular members
u	=	Wave speed
$\dot{u}$	=	Wave acceleration
z	=	Distance from mean sea level

The changing wave height is added using Wheeler stretching, for this the mean sea level is moved to the water elevation, for this the distance from mean sea level is stretched (z'):

$$u(z) \rightarrow u(z') \tag{2.2}$$

The stretched distance from the mean sea level can be calculated as following:

$$z' = d\left(\frac{d+z}{d+\hat{\xi}} - 1\right) \tag{2.3}$$

Where:

d = Water depth
$\hat{\xi}$ = Wave amplitude

To account for the multi-directionality and randomness of waves, a wave spreading factor is applied to the wave speed and acceleration. To define the wave height, long-term wave statistics of irregular waves are used. In chapter 4.1, the input for the wave statistics is explained.
Two important phenomena's that affect the hydrodynamic load on the legs are wave cancellation and reinforcement. Depending on the wave period and incidence angle, the wave height can be different at each one of the four legs. It is possible that the wave crest or wave trough is at all four legs at the same time, then the wave load will be a maximum or minimum (also called wave reinforcement). But there are also cases where this cancels out, this occurs when the wave crest is at two legs and the wave troughs is at the other two legs. In this case, wave cancellation occurs. This will be considered for the selection of the wave heading used in the probabilistic model, as this results in the maximum wave loads.

2.3. Wind load on jack-up

The wind load on a jack-up during offshore wind turbine installation depends on the area that is exposed to the wind. This area consists of the jack-up hull, substructure, crane, legs and the wind turbine components onboard. The number of wind turbine components onboard depends on the vessel size and how many turbines are already installed during the trip, for simplicity, it is assumed that the vessel is fully loaded. Each surface exposed to the wind has its own shape coefficient, defining how the wind flows around the object. In equation (2.4), the formula to calculate the wind load is shown, [9].

$$\vec{F}_{\text{wind}} = \frac{1}{2} \cdot \rho_a \cdot C_s \cdot A \cdot \vec{U}_{wind} \cdot \left|\vec{U}_{wind}\right| \tag{2.4}$$

Where:

ρ_a = Density of air
C_s = Shape coefficient of each component
U_{wind} = Constant wind velocity
A = Area exposed to the wind

In equation (2.4), the whole jack-up needs to be taken into account and the incidence angle of the wind regarding the jack-up orientation. The wind component of the legs between the sea surface and the hull can be neglected, as its contribution is negligible in comparison to the hydrodynamic load on the legs. Only the part of the legs that is above the vessel hull will be considered for the wind load. According to Zhao [29], detailed coefficients for each component are required to be able to include the shielding effects of the different components. For this, wind tunnel tests should be performed to have a good indication of the shielding effects. However, these tests are not available and are deemed too extensive, thus only basic shape coefficients are used.

2.4. Hydrodynamic and wind load interaction

The wind and wave load on the jack-up have different incidence angles, resulting in wind-wave misalignment. Research on the process of blade-root mating, performed by Verma [28], found out that when the wind and wave direction are not aligned, there are more limiting sea states for the crane operations. It can therefore be said that it is of importance to take into account these sea states with misaligned wind and wave directions. It is therefore important to keep a reserve capacity for this wind wave misalignment.

In the industry, limiting environmental conditions for the wave height and wind speed are used. When wind turbines are installed offshore, operators only perform lifting operations when the wave

height and wind speed are below a certain threshold, which are set by the crane manufactures. Current practice, for the threshold, is a significant wave height (H_s) limit of three meters for safe lifting operations. This is the operational limit for the jack-up. For the crane. the operational limit is the mean wind speed. The mean wind speed should be less than 10 to 12 meters per second at 10 meters above sea level, [29]. Above these thresholds, no lifting operations are performed. The chosen jack-up is not yet operational and is expected to be more dynamical sensitive. However, for this research, the thresholds are assumed to be the same, to be able to investigate if these thresholds are still allowable. It may be possible that in the future these limits need to be more conservative due to the increasing dynamical sensitivity of the bigger jack-ups and cranes.

For the external load input into the model, the maximum wind speed and wave height will be based on these thresholds. It is not relevant to take higher wind and wave loads into account, as there will be no lifting operations in those conditions. Operations that are already underway will most likely be aborted if the thresholds are exceeded. It is more relevant to incorporate the wind wave misalignment, as this will result in higher excitation's. However, in this research, wind effects are considered by keeping a reserve capacity in the maximum crane load. This means that the wind wave misalignment will not be considered. This omission is chosen because the induced excitation due to hydrodynamic load is considered to be the main excitation mechanism of the jack-up. The external wind excitation of the lifted loads is chosen to be out of scope.

From the operational limits of the jack-up, it can be concluded that the wave height remains small. For these small wave heights, the wave load is inertia dominated and the drag component can be neglected in the Morison equation, see equation (2.1). When only the inertia component is present, the wave load is linear with the wave height.

2.5. Soil-leg interaction

Numerous researches have been done on modelling the interaction between the soil and the spudcans of jack-ups. Spudcans are the feet of the legs on which the jack-up stands in elevated condition. Most research has been done on jack-ups consisting of three legs, that are used in the offshore oil industry. These rigs are already operating for more than 50 years. Soil interaction is of great interest as a lot of jack-ups incidents and loses are caused due to leg failure induced by punch through of legs. A leg punch through is when the leg reaches a boundary between two types of soil layers. When the lower soil layer is weaker than the top one, there is less soil strength to support the spudcan. When the spudcan reaches this bottom layer, the leg will move rapidly downward. This creates an overturning risk for the jack-up, overturning often results in the loss of the jack-up, [23]. The soil interaction under normal operation has been investigated as this has a significant impact on the jack-up motions. It can be stated that jack-ups, consisting of four legs, do not behave any different when looking at soil interaction as the spudcan and leg load properties remain the same. Hence, each spudcan interacting with the soil can be modelled as a linear elastic spring and damper force in 6 DoF, [5], see figure 2.3. In this way, the soil resistance and damping effects can be included.

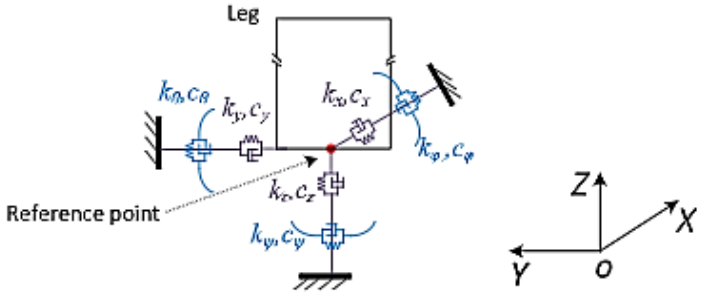

Figure 2.3: Linear spring and dampers to model the soil resistance and damping on the spudcan, [5]

According to Zhao [30], this is an allowable simplification of soil behaviour for jack-up vessels under operational sea states. Because the significant wave height in normal operations remains small, the loads acting on the spudcans do not result in an exceedance of the soil yield surface. The soil reaction

force can be expressed as the following:

$$\mathbf{F}_s = \mathbf{K}_s \cdot \mathbf{X}_{sc} + \mathbf{C}_s \cdot \dot{\mathbf{X}}_{sc} \tag{2.5}$$

Where:

K_s = Soil stiffness vector; $\begin{bmatrix} k_x & k_y & k_z & k_\phi & k_0 & k_\psi \end{bmatrix}$
X_{sc} = Displacement vector; $\begin{bmatrix} x & y & z & \phi & \theta & \psi \end{bmatrix}$
C_s = Soil damping vector

The soil stiffness factor, used in equation (2.5), is dependent on the soil properties and the spudcan penetration and dimension. The location of the components of each vector can be seen in figure 2.3. A correct modelling of the interaction of the footings with the soil is required as the jack-up response to environmental loads is affected by it, [14]. For the simulation of the jack-up dynamic response due to the environment, 5% of the global damping will be used to catch-all possible damping in jack-up. It is assumed that no punch trough occurs, as the loads remain small.

2.6. Leg-Hull connection effects

During lifting operations of the wind turbines, the jack-up is in elevated condition standing on its legs. It is therefore required to look at the connection between the legs and the jack-up hull. This connection consists of a jacking system and a lower and upper guide. The jacking system is used to lift and lower the hull using pinions travelling over a rack and to transfer the shear forces and bending moments from the legs to the hull and the other way around. In figure 2.4, an image is shown of the pinions and rack used to elevate the jack-up. The lower and upper guides also take a part of the bending moment and shear force into account. Therefore, the leg-hull connection needs to be included when modelling the jack-up. This connection can be modelled as a spring with stiffness in all directions. In reality, this connection can show non-linear behaviour due to the possibility of slipping in the gears driving the pinions. Because only small wave loads are considered, it is assumed that these gears do not slip and show linear behaviour.

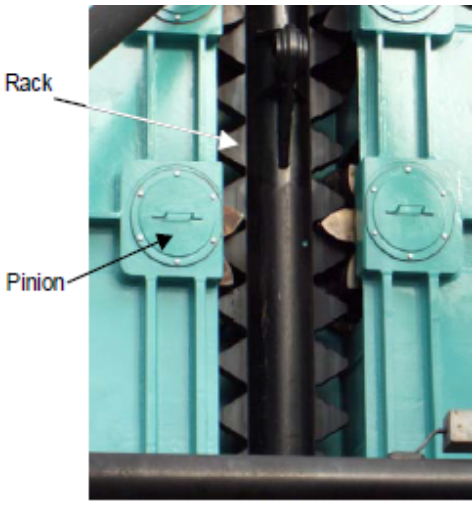

Figure 2.4: Image of a rack and pinion

Another reason to take into account the leg-hull connection is that when the leg is inclined, secondary order effects can occur, [30]. Two types of effects occur, the $p-\Delta$ effect and leg inclination. These two effects create a bending moment in the leg-hull connection. Due to the vertical soil reaction force no longer being in the middle of the leg-hull connection, see figure 2.5. Where P is the reaction force, Δ is the leg offset and M is the resulting moment in the leg-hull connection. In the case of the $p-\Delta$ effect, the leg is bend and the reaction force of the soil is not straight below the leg-hull connection. For the leg inclination, the reaction force of the soil is not in the same direction as the leg-hull connection reaction force. This results in different jack-up dynamic response and lowers the maximum load the

jack-up can handle. Because only small wave loads are considered, these effects are not accounted for in the simulations of the jack-up motions and the legs are assumed to remain perpendicular to the jack-up.

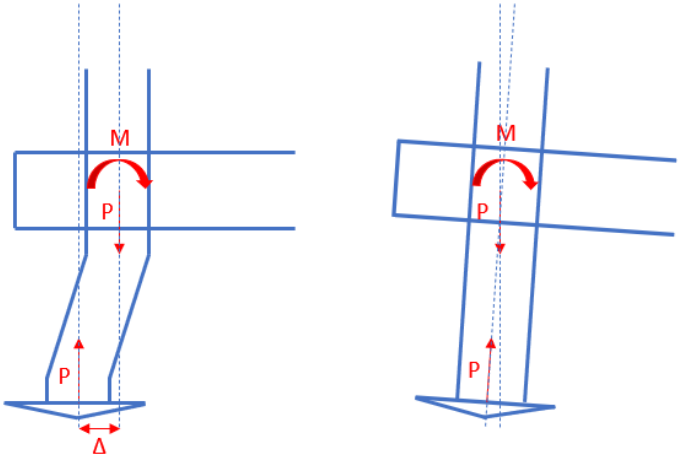

Figure 2.5: Sketch of the $p - \Delta$ effect and leg inclination

2.7. jack-up Crane coupling

When looking at a jack-up which is tasked to install offshore wind turbines, it is necessary to account for the crane dynamic response. The best manner to simulate these dynamic response is to have a combined jack-up and crane model. The crane is a major component of the vessel, which during installation of wind turbines is elevated high above the deck of the jack-up and it can be expected that the crane motions have an influence on the jack-up dynamic response. However, it is preferred to use a stand-alone crane model for simplicity.

In previous research at GustoMSC, two implementation methods have been investigated, [6]. The crane has been modelled as a mass on the deck of the jack-up without accounting for the crane motions. In the other model, the crane has been modelled as a substructure, considering the dynamic response of the crane. It is found that in the model in which the crane is modelled as a substructure, the response is more conservative. Therefore, it is concluded that the model in which the crane is modelled as a substructure is better suited. This allows for the crane dynamics to affect the jack-up dynamics. For the most extreme displacement cases, it was found that when the crane is modelled as a substructure, the jack-up displacement is damped. According to Engelen [6], this makes the option of having a stand-alone model of the crane not possible, as this damping would not be incorporated correctly. However, this is for the investigation of dynamic response due to earthquakes, where transients occur. In this research, a steady-state is investigated and the damping of the jack-up motions due to the crane is not relevant.

It can be concluded that it therefore acceptable to use a stand-alone model of the crane where jack-up motions are fed into. In chapter 3, the onboard heavy lift crane and its characteristics will be discussed and in chapter 5 the time-domain simulation models of the jack-up and the crane are discussed.

3

Heavy lift cranes used for offshore wind turbine installation

This chapter discusses the different aspects of the heavy lift cranes mounted on jack-ups, used to install offshore wind turbines. Only luffing boom cranes are considered for this thesis. The cranes used on jack-ups are leg encircling, which means they are built around a jack-up leg to minimize the required deck space. To start, the chosen reference crane will be shown and its properties will be listed. Next, the installation procedure of offshore wind turbines is discussed. The crane boom hoist wire rope and hoist wire rope dynamics are revieuwed. Multiple different configurations of the load in hook are investigated and the most relevant configurations are chosen for the model. The different types of bearings in the crane are investigated and the influence of eccentricity in the load in hook on the sling dynamic response is investigated. Below, the different items are listed:

1. Crane properties
2. Wind turbine installation procedure
3. Crane wire rope modelling
4. Bearings in the crane
5. Non-linear sling coupling

3.1. Crane properties

First, a general arrangement of a heavy lift crane used on jack-ups is shown in figure 3.1, with the different components highlighted. A crane with a 2000 ton lifting capacity, at 45 meters radius, is chosen for this thesis, in table 3.1, the dimensions are listed. The crane boom has a length of 167 meters and a maximum luffing angle of 75 degree, which gives a maximum lifting height of 220 m above sea level. This height includes the crane pedestal and the jack-up elevation above sea-level.

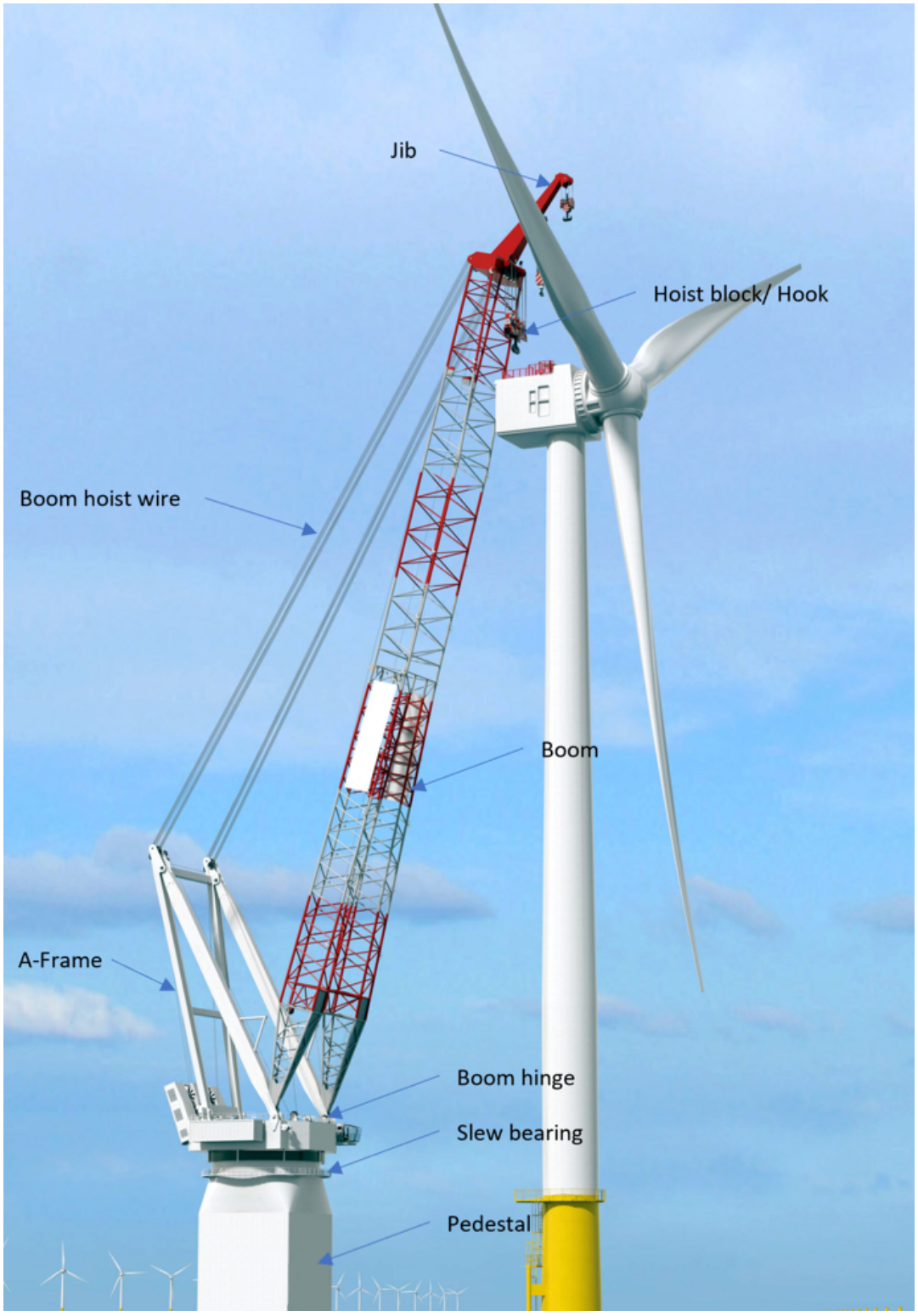

Figure 3.1: Image of a typical offshore heavy lift crane, with the different components explained, [21]

Table 3.1: Dimensions of the chosen crane

Crane parameter	Value
Boom length [m]	167
Boom mass [ton]	1050
Capacity @45m [ton]	2000

In figure 3.2, the coordinate system of the crane is shown. The origin of the coordinate system is at the heel point of the crane. The luffing angle can be seen in the stern view of the jack-up, figure 3.2a,. In the top view, the slewing angle can be seen, figure 3.2b.

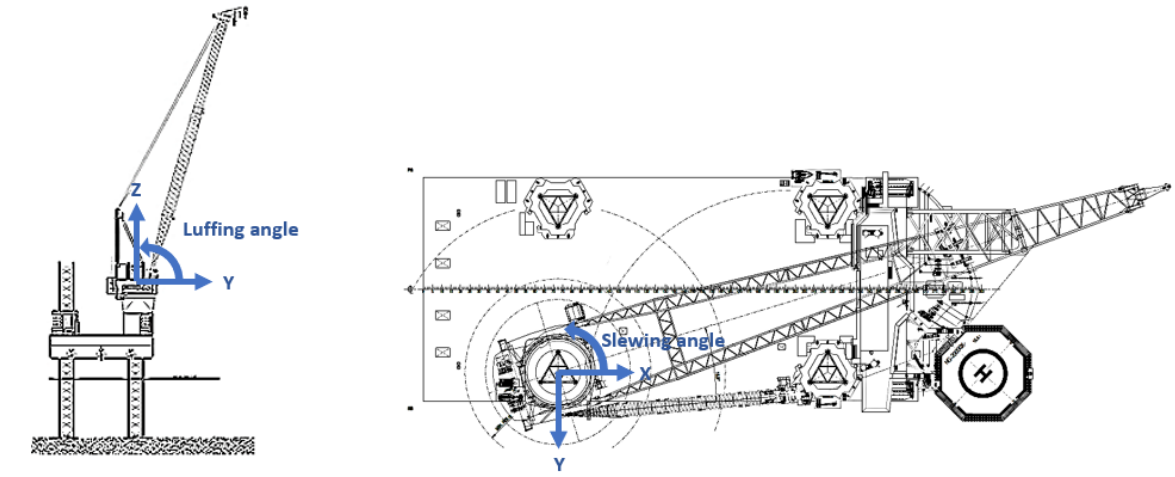

(a) Coordinate system of the crane, stern view

(b) Coordinate system of the crane, top view

Figure 3.2: Coordinate system of the crane, stern and top view

3.2. Wind turbine installation procedure

Over the years, different installation procedures have been attempted for the installation of offshore wind turbines. In figure 3.3, multiple common installation methods are shown. Currently, most offshore wind turbines are installed according to method two. For the installation of 20 MW wind turbines, it is assumed that the same method will be used as current practice. Method two is also used in the installation campaign, of which the measurement data is available. This requires to consider five lifts, a tower lift, a nacelle lift and three blade lifts, per installed wind turbine.

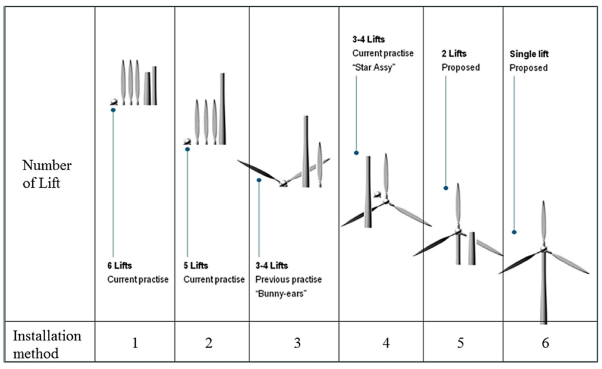

Figure 3.3: Different installation methods, [2]

For the installation of the wind turbine blades, it is common practice to use tugger lines to control the load in hook dynamics. For this research, these tugger lines are neglected as these are not incorporated in the NX-motion model.

3.3. Crane wire rope modelling

An important part of a crane, are the wire ropes used to lift the boom to the required luffing angle and to lift the load in hook. Multiple researches have been performed on how to model wire ropes (steel cables) and their behaviour under varying loads. Below, two possible modelling ways will be reviewed. As can be seen, in figure 3.1, the cranes used for wind turbine installation using a jack-up consist of a boom connected to the A-frame by a hinge at the bottom and wire ropes at the top. These ropes are used to control the luffing angle of the boom. The boom hoist wire rope of a typical heavy lift crane consists of two wire ropes which are reeved multiple times, this ensures that the load is evenly distributed over each reeve. Next to that, wire ropes are used to hoist the loads in the hook. These ropes are reeved around several sheaves to create multiple reevings. This ensures that the load is divided over multiple reeves and reduces the load in each wire rope. At the top of the crane there are multiple sheaves as well as in the hoist block to which the hook is connected.

The wire ropes used in offshore heavy lift cranes, are made up of multiple inner wire ropes. Between these wire ropes, internal friction occur, which needs to be considered in the crane model. When the rope is loaded, the rope will be elongated and friction will occur between the different wire ropes and the same occurs when the wire rope is unloaded. This results in dissipation of energy within the material, also referred to as internal damping. When modelling the wire ropes in the model, these effects need to be considered. According to Velinsky [24] and Van der Valk [22], wire rope stiffness can be modelled as a spring force which can be assumed to be linear with the elongation, see equation (3.1).

$$F_{linear} = \frac{E \cdot A \cdot C_f}{L} \cdot \Delta L \tag{3.1}$$

Where:

F_{linear}	=	Linear spring force
E	=	Elasticity modulus of steel wire rope
A	=	Area of the boom hoist wire rope
L	=	Total length of the boom hoist wire rope
ΔL	=	Elongation of the wire rope
C_f	=	Fill factor of the wire rope

Another method of modelling the wire ropes is to use the Bouc-Wen model. This model is based on hysteresis, which means that for each cycle of loading and unloading energy will be dissipated. But that the amount of damping is dependent on the direction. So, when the wire rope is loaded, the damping is different, to when the wire rope is unloaded, see figure 3.4, where a hysteric damping cycle is shown. The area enveloped by the hysteresis curve, is the energy dissipated in each cycle.

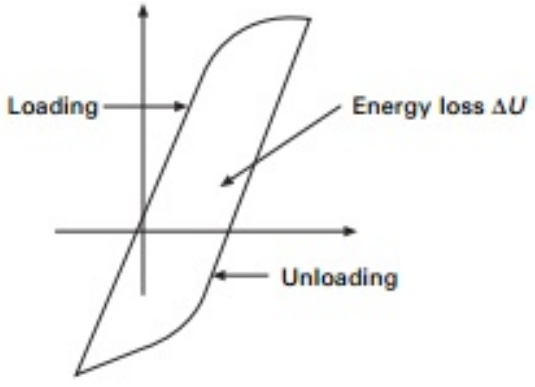

Figure 3.4: Hysteresis loop for damping, [15]

According to Haniszewski [8], this way of modelling wire rope is well suited to model dynamic states during lifting, like impact loads. For lifting operations when the rope is always tight, the Bouc-Wen model performs similarly to the linear elastic model. It is then preferred to use the linear elastic model for simplicity. In the to be used NX-motion model, the hoist wire rope is modelled as a rigid body with

a damper at the crane tip. For the boom hoist wire rope model, further research is performed, this is shown in section 3.3.1.

3.3.1. Mass modelling of the boom hoist wire rope

The boom hoist wire ropes have a considerable mass in comparison to the crane boom itself, the crane boom weighting 1150 ton and the boom hoist wire ropes around 80 ton. In the case the wire rope is modelled as a linear spring, the weight of the boom hoist wire rope is neglected. It is possible that due to the mass of the wire rope, catenary effects occur when the wire rope is sagging. This means that the wire rope is not completely in tension due to the load hanging in the crane top. Due to the out-of-plane motion of the crane tip, the catenary effect can influence the dynamic response of the cane. If the wire rope is fully tensioned, it can be assumed that the mass of the wire rope has no influence on the dynamic response of the crane and that the wire rope can be modelled as a spring. To incorporate this mass, it is possible to model the wire rope as multiple mass spring elements. For this, the wire rope is divided into multiple elements. Each element is modelled as a spring to which at both ends a mass point is located, accounting for the mass of each wire rope section, see figure 3.5. This method is used by Koole [12], to investigate stress waves in the event of wire rope failure.

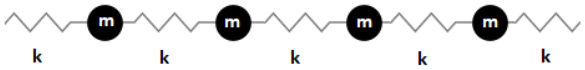

Figure 3.5: Mass spring set-up used in the investigation

It is investigated if incorporating the boom hoist wire rope mass results in catenary effects. For this, a model is built that divides the wire rope in mass-points connected to each other by springs. In figure 3.6, the set-up of the model is shown. The tension in the wire rope is investigated for multiple loads in the hook and luffing angles. The three loads are, only the hoist block without load in hook, 50% of lifting capacity and the maximum lifting capacity of the crane. The luffing angles are fully luffed, at 45 degree and 5 degree. In the case the boom is fully luffed, all three load cases will be considered. The crane is luffed at 5 degree when it is being lifted out of the hoist block. In these two cases, the only load in the crane is the weight of the hoist block, as no lifting operations are performed at these luffing angles.

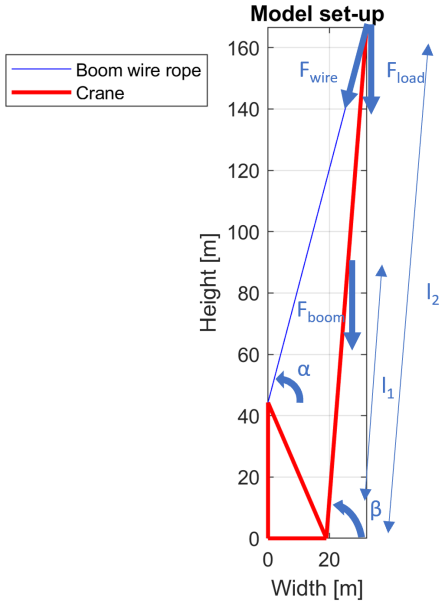

Figure 3.6: Model set-up for the investigation of the catenary effects in the boom hoist wire rope

The applied force in the hoist wire rope due to the mass of the boom and the load in hook is calculated

as following:

$$F_{wire} = \frac{F_{boom} \cdot l_1 \cdot cos(\beta) + F_{load} \cdot l_2 \cdot cos(\beta)}{l_2 \cdot cos(\alpha) \cdot sin(\beta) - l_2 \cdot sin(\alpha) \cdot cos(\beta)} \quad (3.2)$$

Where:

α	=	Angle of the boom hoist wire rope
β	=	Luffing angle
F_{boom}	=	Force due to the mass of the boom
F_{load}	=	Force due to the load in hook
F_{wire}	=	Force in the wire rope
l_1	=	Distance from hinge to COG of the boom
l_2	=	Boom length

The different variables, used in equation (3.2), are also shown in figure 3.6. The calculated wire rope force is then applied at the crane tip in the model. Using this force, an equilibrium is searched for the boom hoist wire rope. In figure 3.7, the wire rope is shown for the case where the boom is fully luffed and the three different loads are applied. As can be seen, the sagging that occurs is negligible for the three cases.

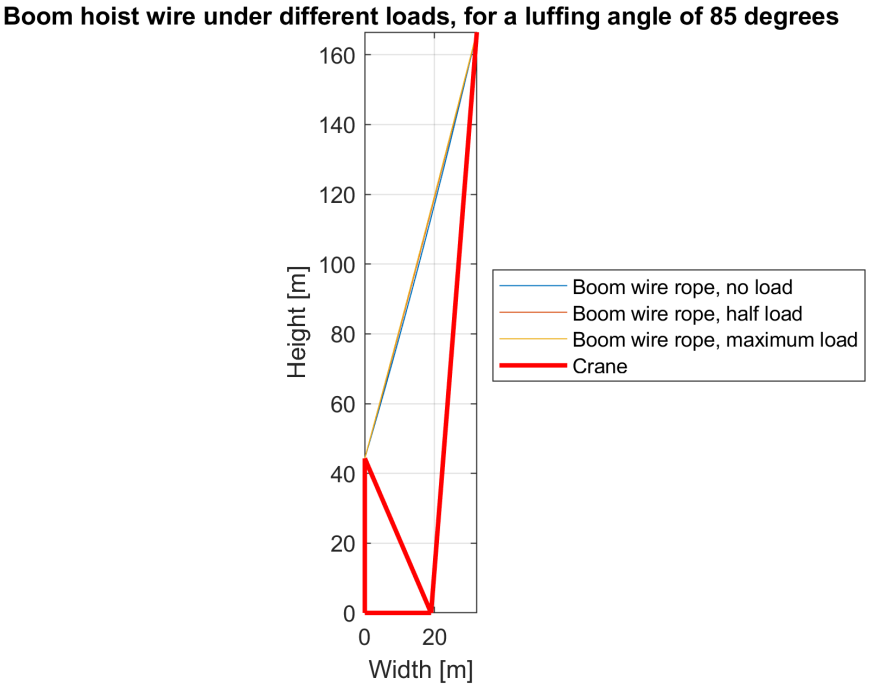

Figure 3.7: Boom hoist wire rope, when the boom is fully luffed

In figure 3.8, the boom is luffed at an angle of 45 degree and the catenary boom hoist wire rope is shown. From the figure, it can be concluded that the sagging is negligible.

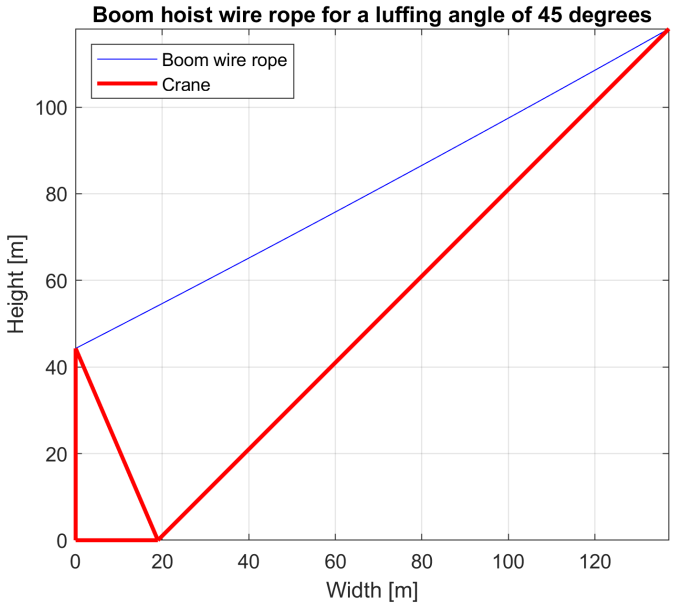

Figure 3.8: Boom hoist wire rope, when the boom is luffed at 45 degree

At last, in figure 3.9, the boom hoist wire for a luffing angle of 5 degree can be seen. Like for the other two luffing angles, negligible sagging occurs.

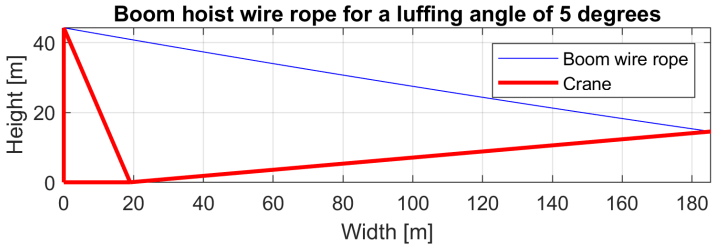

Figure 3.9: Boom hoist wire rope, when the boom is luffed at 5 degree

No sagging of the boom hoist wire rope occurred for the different applied loads and luffing angles. It is therefore concluded that in all the different configurations, the sagging of the boom hoist wire rope can be neglected. It can therefore be concluded that the boom hoist wire rope is under tension. Looking at how this influences the dynamic response of the crane, it can be said that when the crane tip moves out-of-plane, the effect of the boom hoist wire mass is non-existent. Therefore, there is no damping or excitation of the crane boom due to catenary effects of the boom hoist wire rope. Furthermore, the Bouc-Wen model is not applicable, as no impact loads are expected in the boom hoist wire rope. These impact loads do not occur, as this research focuses exclusively on crane failure under normal operations. Therefore, the boom hoist wire rope will be modelled as a spring.

3.3.2. Hoist wire rope dynamics

Currently, a simple pendulum is used to model the load in hook. However, it is investigated how a more representative modelling of the load in hook will affect the dynamic response of the sling. If, for example, the sling fundamental natural period is close to the wave excitation period, resonance will occur. This will increase the load in the crane tip and have an effect on the dynamic response of the crane. For the following calculations, hoist wire rope elongation will be omitted, the hoist wire rope will be assumed inextensible. Next to that, damping of the load due to drag will be disregarded. The damping due to drag is especially high for wind turbine blades, as these are light structures and have a big surface. This also makes wind turbine blades more prone to be excited by the wind. But for the simple calculation below, it is too complex to take the drag and wind excitation into account.

Hoist wire rope configurations investigation

Common practice for the hoist wire rope is to model it as a simple pendulum, it is investigated if this simplification is acceptable. In reality, the hoist configuration consists of a hoist wire rope with a hoist block at its end. The hoist block has a hook to which a hoist tool is attached. For each different wind turbine component, a different tool is used. Namely, a tower tool, a nacelle tool and a yoke for the blade installations. Therefore, a double pendulum would be a more detailed representation of the hoist configuration, for configuration with a high load in hook. It is investigated how different configurations affect the dynamic response of the hoist wire rope configuration.

The hoist wire rope dynamic response is dependent on the sling length, load size, load shape and the hoist block. There are more parameters, but only the ones mentioned will be taken into account. It is also known that, for example, in some lifting operations an offset in the COG of the load could occur, which could affect the dynamic response of the hoist wire rope. In section 3.5, it is investigated if non-linear couplings occur when the COG of the load has an offset.

Four configurations are investigated, the first one is a simple pendulum, thus a sling with a point mass at its end. The second configuration consists of two slings coupled by a hinge and a distributed mass attached at the bottom of the second sling. The next configuration has a sling to which a distributed mass is attached at its end. The fourth configuration is a sling to which at its end a hoist block is attached, modelled as a point mass, to which another sling is attached. At the end of this last sling there is a distributed mass. This can be seen as the most complete configuration as it represents the hoist block and the load in hook. For all four configurations, the COG of the loads is kept at the same distance from the crane tip. This configuration represents, for example, the lifting of a tower. In figure 3.10, the four different configurations are shown. Where, L is the sling length and M the mass of the load.

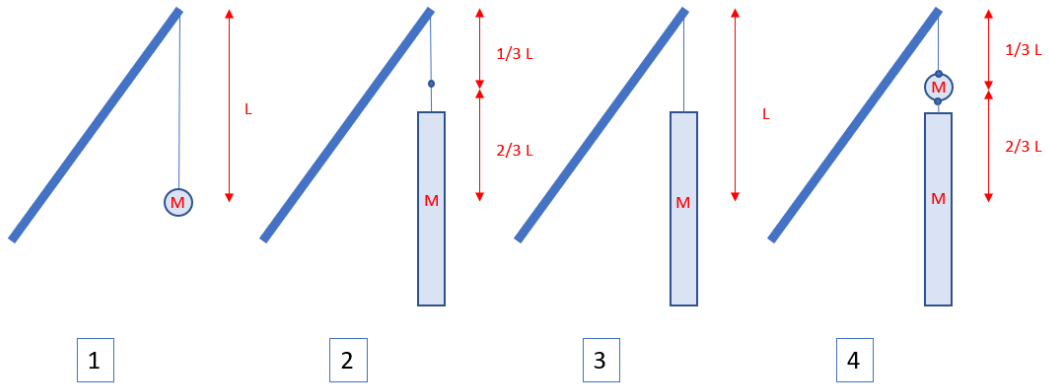

Figure 3.10: The four pendulum configurations

For the calculation of the fundamental natural period of a simple pendulum, like configuration 1, the following equation applies:

$$T_{nat} = 2\pi\sqrt{\frac{L}{g}} \tag{3.3}$$

Where:

L = Length of the sling
g = Gravity

For the third configuration, the point mass is replaced by a distributed mass which has a moment of inertia, for this, equation (3.3), has to be modified. In this equation, the sling length L becomes $\frac{I}{M \cdot R}$ where I is the moment of inertia of the load, M is the mass of the load and R is the distance between the pivot point and the centre of mass. In this case, R is equal to the sling length, which is the same as in configuration one. Configurations two and four cannot be described as simple pendulums and are solved using Lagrange. For these configurations, general formulas can be derived using Lagrange for the fundamental natural period of the different configurations. These formulas are dependent on the sling length, the mass ratio between the hoist block and load in hook and the inertia moment of the load in hook. In appendix A, the mentioned general formulas, for the four configurations, can be found.

To be able to compare the results, the distance between the COG of the load in hook and the crane tip is the same for the four configurations. In table 3.2, the fundamental natural period for each configuration is shown. It can be noted that the configurations with an extra hinge have higher fundamental natural periods than the ones without. Adding more detail to the sling configuration increases the fundamental natural period. Therefore, the currently used sling configuration (configuration one) is conservative.

Table 3.2: Fundamental natural period for the different pendulum configuration

Configuration	1	2	3	4
T_{nat} [s]	14.2	18.6 - 24.7	16.7	18.5 - 23.8

Conclusion of the hoist wire rope configurations investigation

The fundamental natural period of configuration one and three are relatively close to each other. For configuration three, the fundamental natural period is a bit higher due to the added inertia of the load. Configuration two and four have almost similar results, this small difference is due to the mass of the hoist block at the hinge. It can be concluded that the effect of modelling the hoist block is negligible. To account for this effect, the mass of the hoist block is added to the mass of the load in hook. It can be concluded that adding detail to the model of the sling affects the fundamental natural period of the sling by increasing it.

In the crane model, currently, configuration one is used in the crane model. If another configuration is chosen, it would need to be validated and this is out of scope for this research. The change in fundamental natural period between the different configurations, results in a change of acceleration of the load in hook. This changes the loads in the crane, to account for this, the sling length of configuration one is being scaled to match this difference. It is concluded that to account for the difference in fundamental natural period between the currently used configuration and the configuration with more detail, the sling length will be changed.

3.4. Bearings in the crane

In the cranes, used to install offshore wind turbines, multiple types of bearings are used. These are the sheaves for the cables, the hinge around which the crane boom can luff and the slew bearing to rotate the crane around the leg. Below, for each type of bearing, the modelling approach and simplifications will be discussed.

3.4.1. Reeving sheaves friction

The boom hoist wire rope and the hoist wire rope are reeved multiple times. For each reeve, sheaves are used around which the wire rope can rotate. Sheave are present in the hoist block, crane tip and at the top of the A-frame. These sheaves experience friction when rotating. The friction at the sheave comes from the shaft and the pin around which the sheave rotates and due to the bending of the wire rope around the sheave. The friction at the pin around which the sheaves rotate comes from the load in the wire rope, which will hang on the pin. When the wire rope bends, friction occurs within the wire

rope between the different inner wire ropes. To account for this, DNVGL [26], states that 2% friction needs to be considered for each sheave. This friction is only relevant to the required lifting force and cannot be seen as a damping force of the structure. Consequently, it will not be considered as it is not essential for the dynamic response of the crane.

3.4.2. Crane boom hinge friction

The hinge of the crane is the bearing connection between the crane boom and the crane house. The hinge consists of a PTFE tube around a pin that is connected to the crane house and encircled by the crane boom. Due to the mass of the boom on the bearing, friction occurs. This friction can influence the dynamics of the boom and the transfer of dynamics between the jack-up and the crane. Koole [12], investigated friction at the hinge of a 10 000 ton lifting capacity crane where the bearing is made of bronze, with a friction coefficient of 15%. Common practice in cranes, is to use a PTFE layer, which has a friction coefficient of 10%. The maximum force in the boom hoist wire rope for friction coefficients ranging from 0 to 100% is investigated by Koole [12]. It is found that the effect of friction of the hinge is small on the force in the boom hoist wire rope and is thus negligible. No further research is found about boom hinge friction and the effects on the dynamics response. Thus, it will be assumed that the friction that occurs at the hinge is negligible and is not taken into account for the modelling of the crane.

3.4.3. Slew bearing of the crane

The cranes on jack-up vessels for the installation of offshore wind turbines are generally leg encircling. This means that the crane pedestal is located around a leg. On this crane pedestal, a slew bearing is located, making it possible for the crane to rotate around the leg. No research is found about possible friction or other dynamic effects for the slew bearing of cranes. Koole [12], Van der Valk [22] and Daalen [4], made dynamic models of offshore cranes including the slew bearing of the crane. Only the overturning moment in the slew bearing was incorporated. In these models, it is assumed that no friction occurs in the slew bearing of the crane. In the NX-motion model the overturning moment in the slew bearing is not relevant and the crane dynamic response are investigated at fixed slewing angles. Therefore, the friction in the slew bearing is discarded.

3.5. Non-linear sling coupling

During the lifting of a wind turbine component, it is possible that the centre of gravity (COG) of the load is not directly below the crane tip or has an offset. In this case, extra coupling effects can occur. This is investigated using the crane model in NX-motion, this model is described in chapter 5. To investigate the effect of coupling of the load in the sling, two different configurations of the load in the sling are modelled in NX-motion. The first configuration is a point load hanging in the sling which has its COG located directly below the crane tip, see figure 3.11a. The second configuration, models a tower lift where the COG has an offset and has an inertia around the z-axis, see figure 3.11b and 3.12. In figure 3.12, it can be seen that the COG of the load has an offset. The COG is located at the local axis system that can be seen in the figure. The COG of the load is located at half the boom length below the crane tip and the luffing angle is taken to be the maximum allowed luffing angle.

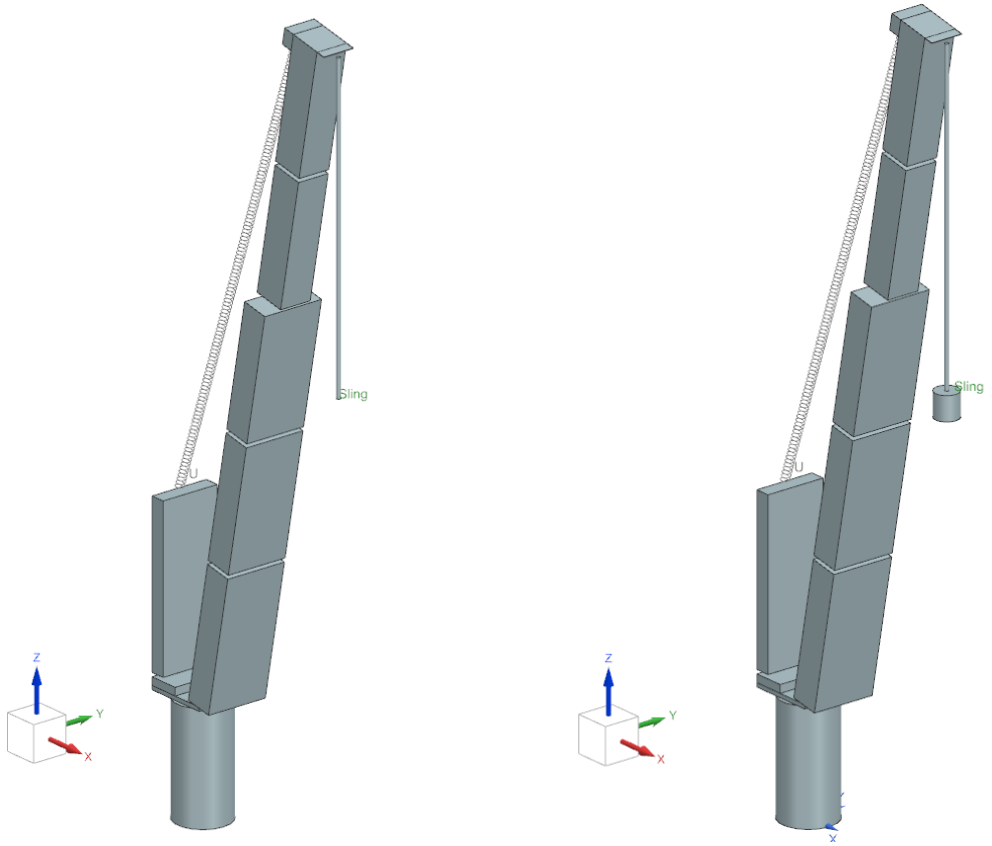

(a) Crane model with a point load at the end of the sling

(b) Crane model where a tower is modelled with eccentricity in the load

Figure 3.11: Comparison of the two different models

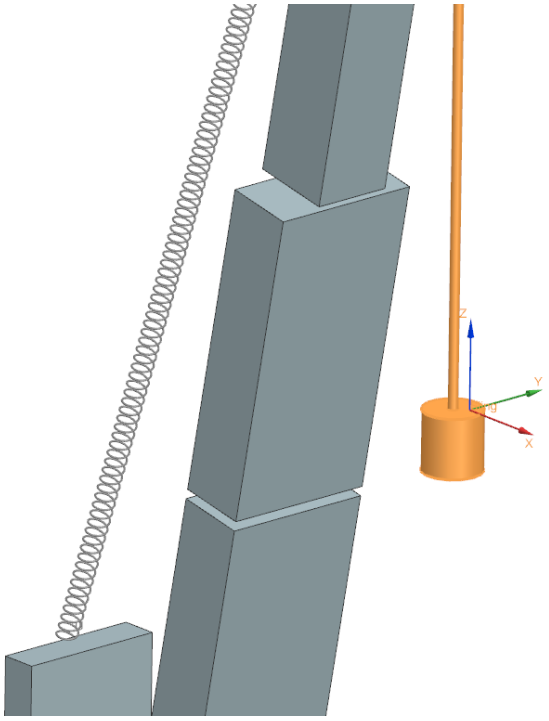

Figure 3.12: Zoom in of the tower hanging in the sling, with the COG eccentricity shown

To investigate the difference in dynamic response of the two configurations, a white noise signal is used as input to simulate the jack-up motion. Using a white noise signal will excite the crane at all possible frequencies and is much higher than the expected wave excitation. The input is split into a component in the x-direction or y-direction, to identify the coupling. Both noise inputs are run separately, to be able to distinguish if excitation occurs in the perpendicular direction. In equation (3.4), the relation between the input and output displacement of the load in hook is shown.

$$\begin{bmatrix} U_{x,\text{ out}} \\ U_{y,\text{ out}} \end{bmatrix} = \begin{bmatrix} H_{xx} & H_{xy} \\ H_{yx} & H_{yy} \end{bmatrix} \cdot \begin{bmatrix} U_{x,\text{ in}} \\ U_{y,\text{ in}} \end{bmatrix} \tag{3.4}$$

Where:

U_x = Displacement in x-direction that is the input (in) or output (out) of the model
U_y = Displacement in y-direction that is the input (in) or output (out) of the model
H = Transfer function, where x and y represent the direction

In table 3.3, the significant amplitudes of the two configurations are shown. It can be remarked that, as expected in the case of no offset, no coupling occurs. The significant amplitude of the off-diagonal terms are almost zero. In the case of an offset, there is a small coupling, but its amplitude is negligible compared to the amplitude in x- or y-direction. So, no coupling occurs when there is an offset of the COG in the load, hanging in the sling, during a lifting operation.

Table 3.3: Significant amplitude of the coupling terms of both models

Term	Sling model; significant amplitude	Tower model; significant amplitude
H_{xx}	33.987	65.466
H_{xy}	1.086e-10	0.007
H_{yx}	0.095	0.527
H_{yy}	44.780	117.829

In the model, it is assumed that the load has no offset and no coupling occurs during lifting operations. This is acceptable as it is found that in the case there are off-diagonal inertia terms, no coupling effects take place in the dynamic response of the load. The load in hook is modelled as a point load without any off diagonal inertia terms.

4

Model input

In this section, the required inputs of the time-domain simulation models are investigated. Three different components are looked at for the input, these are listed below:

1. Environmental input
2. Jack-up configurations
3. Crane configurations

The environmental input for the jack-up model is described, for this multiple locations are looked at. The different configurations, of the jack-up and the crane, will be defined. These configurations will be used as input for the model. Next to that, different lifting operations are considered for the crane. Each lifting operation has different luffing and slewing angles. Moreover, the sling length and load in hook is dependent on the component being lifted. For this, a given data set of measurement data of a crane on a jack-up is investigated. This data was recorded on another jack-up than the one used in this thesis. This jack-up is smaller and has another deck layout and crane location, so the data is translated to the used jack-up size, deck lay-out and crane location. At last, a selection is made of the relevant crane configurations to be used as input for the simulations.

4.1. Environmental input

Jack-up dynamic response is wave load dominated, and therefore it is of great importance to model this correctly into the time-domain simulation model. It is chosen to only take the wave loading as environmental loading and discard the current and wind loads. To be able to calculate the wave load on the jack-up legs, wave statistics are required. These wave statistics will give input to the time-domain simulation of the jack-up in SIMSEP. For more information about SIMSEP, see section 5.1.

For the model, the wave spectra, defined by DNV [25], will be used. These spectra are based on long-term wave statistics of the selected regions. The long-term statistics give the probability of occurrence of each combination of H_s and mean zero-crossing period (T_z) combinations. For each region, multiple parameters are defined which, respectively, represent the Weibull parameters and log-normal distribution parameters for H_s and T_z. Using a general formula, the wave scatter diagram of the selected region can be made. This is required because each sea-state is different and based on these parameters this can be taken into account. To get a general representation of the wave statistics, multiple locations are considered. These locations are where currently most offshore wind turbines are being installed. The jack-ups operations are not limited to only one region and to exclude that other wave statistics apply in the different regions, all these regions are considered. For this thesis, 5 regions are investigated, these 5 regions are a good representation of where the most offshore wind turbines are currently being installed:

1. North Sea
2. Atlantic coast of France
3. West coast of Taiwan
4. East coast of Taiwan
5. East coast of Japan

The mean probabilities of the five regions is taken. In figure 4.1, the long-term wave statistics are shown, the occurrence of the H_s and T_z are shown for the five regions mentioned above.

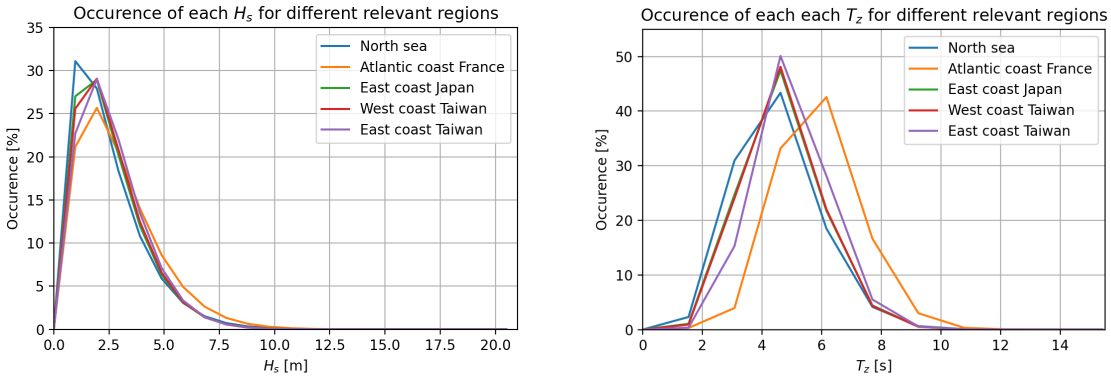

(a) Probability of the occurrence of the H_s for the different regions

(b) Probability of the occurrence of the T_z for the different regions

Figure 4.1: Probability of occurrence of the H_s and T_z for the selected regions

The spectrum of the Atlantic coast of France is omitted, as the T_z distribution is significantly different in comparison to the other distributions. The difference in T_z probability is caused by the fact that this region is more swell dominated. For simplicity, only the other four locations will be used, as their spectra are similar. Moreover, as stated in section 2.4, the maximum significant wave height in which lifting operation are conducted is 3 meters. So higher significant wave heights are not relevant for this research, in figure 4.2, the new distributions are shown for wave heights of 3 meters and lower and without the Atlantic coast of France statistics.

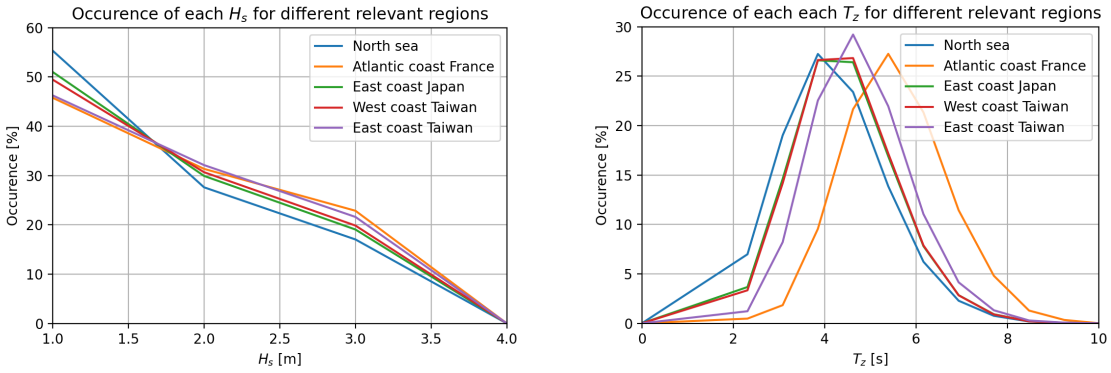

(a) Distribution of the occurrence of the H_s

(b) Distribution of the occurrence of the T_z

Figure 4.2: H_s and T_z distribution with a maximum significant wave height of 3 meters

For the input of SIMSEP, the peak period (T_p) is required, instead of T_z. The relation between the two periods, for a peak enhancement factor (γ) of 3.3, is:

$$T_p = 1.298 \cdot T_z \tag{4.1}$$

So the chosen $H_s - T_z$ combinations, defined by DNV [25], are transformed to $H_s - T_p$ combinations.

4.2. Jack-up configurations

The jack-up can be configured in multiple ways, the operational loading depends on three components. The chosen type of jack-up used in the simulation, is in this case a NG-20000X wind turbine installation jack-up. The dimensions of this jack-up are listed in chapter 2. The following three aspects of the chosen jack-up can vary:

1. Water depth
2. Wave heading
3. Elevated weight

The water depth in which the jack-up is operating can differ depending on the location of the wind farm. In this case, three water depths that represent the most common depths, for this jack-up, will be investigated. These water depths are 40, 50 and 60 meters, with the same probability of occurrence.

During the installation of offshore wind turbines, the wave heading relative to the jack-up can vary. The heading of the jack-up in relation to the environment is defined by the specific site conditions. Often, the location where the jack-up jacks-up depends on the limitation set by cables on the sea floor and previous jack-up that jacked-up (old leg footprints). Because it is not possible to consider all the wave headings, the headings which are expected to result in the most dynamic response are used. These headings are expected to be when the effects of wave cancellation and reinforcement are the most distinguishable, see section 2.2.1 for more explanation about this subject. This is when the wave heading comes head-on, on the beam and on the leg-diagonal (0, 90 and 56 degree wave heading). It is assumed that during the installation period of one wind turbine, the probability of the wave heading coming from one of the three headings is the same. Moreover, it is assumed that the wave heading does not change during a lift of a component. In section 4.3.2, it is found that no lift has a longer exposure time than a sea-state of 3-hour.

Jack-ups take components for multiple wind turbines at once. During an installation trip, the elevated weight varies for each installation. For this thesis, it is assumed that the elevated weight remains the same for each lift. The maximum elevated weight is taken for all the jack-up configurations.

4.3. Crane data interpretation

Another important input for the model is the crane configuration. Each different crane configuration will result in a different dynamic response. For this, the crane operations of a jack-up installing wind turbines is investigated. Current practice for the installation of offshore wind turbines has been identified in section 3.2. To identify the different crane operations, a measurement data set is made available of a smaller jack-up. As stated in section 2, a NG-20000X is used in this research. Therefore, the measured data needs to be translated to the correct jack-up lay-out. From the data-set, the crane orientation, loads in the hook and the occurrence of these configurations can be retrieved. The exposure time of the different lift types are investigated. At last, the relevant configurations are listed that are used as input for the crane and probabilistic model.

4.3.1. Operational profile of the crane

The occurrence and exposure time of the different types of lifts is retrieved from the set of measured data. This data-set consists of measurements for each second that the crane is operating and a load is in the hook. When there is no load in hook, there is no recorded data. The time-span of the measurement data is 60 days, during which 13 wind turbine installations have been performed. The installed wind turbines have a capacity of 6.3 MW. When extrapolating this to a 1-year period, where the required installation time per turbine is taken to remain the same, a total of 82 turbines are installed. This is neglecting maintenance downtime of the jack-up and assuming that the transit time between the wind park and the harbour remains the same. Furthermore, the measurement data is of a wind park installed on the East coast of England, from October until December, which are harsher months in terms of environmental conditions. This could mean that the installation time per turbine is conservative, as in more benign months the installation rate can be higher. It is important to note that the lifts that occur in the sheltered waters of the harbour, where the wind turbine components are loaded onboard the jack-up, are neglected in this research, as the wave load will be negligible. Moreover, the lifting of other tools than the yoke and of other equipment is assumed to be non-relevant for this

research. The loads are expected to be negligible in comparison to lifting the heavy components of the wind turbine. An important limitation of the available data-set, is the small amount of measured lifts. Anomalies in lifts can have a significant impact on the used input of the probabilistic model. This is especially important for the exposure time of the lifts that can vary a lot, see section 4.3.2.

During lifting operation, the crane rotates around the leg and the crane boom is raised and lowered. To be able to quantify the occurrence of each crane set-up, the described measurement data is used. In figure H.1 and H.2, the occurrence of each slewing and luffing angle is shown in a radar plot. It can be remarked that the crane boom is mostly luffed between 75 and 85 degree, which is the angle at which the wind turbine components are picked-up and installed. The crane is generally slewed above the boom rest. This is because most operations occur in this area, the boom is luffed out of the boom rest to the required luffing angle. Furthermore, most of the wind turbine components are also located between the accommodation and the crane pedestal, see figure 4.3. The crane is also slewed outboard, this is to install the components. The three main angles outboard are at 40, 90 and 130 degree. The location of the tower and nacelle is at 130 degree. The crane's other outboard slewing angles are where the blades are installed.

The deck layout of the reference jack-up can be found in figure 4.3 and of the NG-20000X jack-up can be found in figure 4.4. The different wind turbine components are shown, as well as the location of the crane and the tools. The main differences between the two deck layouts, is that the crane is located around the starboard aft leg of the NG-20000X jack-up and of the reference jack-up around the portside aft leg. The blade rack is moved from the bow to the stern of the jack-up in the chosen jack-up. All the towers and nacelles are located in front of the crane instead of on both sides of the crane. The tools required for lifting the different components are stored in between the two aft legs instead of the stern where, as mentioned, the blade rack is now located. The total number of wind turbines onboard remains the same, even with a much bigger size the NG-20000X cannot carry more wind turbine than the smaller reference vessel because the 20 MW wind turbine are much heavier and larger than the 6.3 MW wind turbine installed by the reference jack-up.

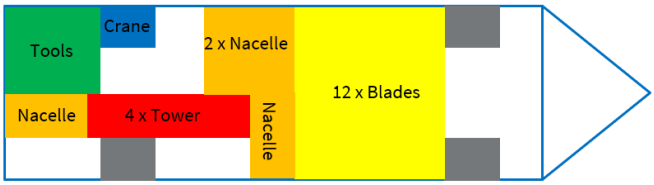

Figure 4.3: Layout of the deck of the reference jack-up with the different wind turbine components and tools

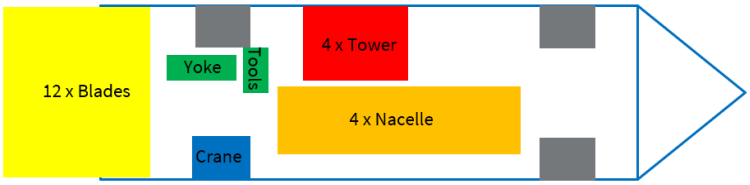

Figure 4.4: Layout of the deck of the jack-up with the different wind turbine components and tools

Using the described deck layouts above, the measured data of the reference jack-up has been used and converted to the deck layout of the used jack-up. For this, the measured slewing and luffing angle of each lift type have been investigated. From this, the distribution of the slewing and luffing angle have been translated to the new deck-layout. The translated slewing and luffing angle of the crane can be found in figure H.3 and H.4. In appendix B the radar plots of the slewing and luffing angle of all the different lift types can be found. The different lift types are; tower, nacelle, blade and yoke lift. The main difference that can be seen is that a peak appears facing the stern of the vessel and that the peak above the boom rest is smaller, this is due to the new location of the blade rack at the stern of the vessel. Moreover, a more pronounced peak is at 90 degree, where all the tools are now located. The distribution of the luffing angle remains the same because the relative distance of the wind turbine components to the crane pedestal remains the same.

4.3.2. Exposure time of the crane

Now that the slewing and luffing angle of each different lift have been investigated, the exposure time of these lifts needs to be defined. For this, the exposure time of each lift is identified in the measurement data. In appendix B, a representative time-trace of each type of lift is shown. The slewing angle, luffing angle, load in hook and hook travel are shown over time. From the dataset, each exposure time is retrieved. For each lifting type, a cumulative density function (CDF) is fitted over the data and the best statistical distribution is investigated. A Weibull distribution is chosen as the best fit of the data. In figure H.5a, H.5b, H.6a and H.6b, the histogram for each lift type is shown, as well as the probability density function (PDF). The PDF is shown, as this gives a better visualization than a CDF. Given that there are only 13 measured wind turbine installations, the fit of the distribution of the exposure time is quite rudimentary. For more accuracy, a larger data set with more wind turbine installations, would be better. For now, the less accurate fit is used as no more measured data is available.

It can be remarked that the distribution of the exposure time of the blade and yoke lift is wide compared to the tower and nacelle lifts. This can be explained by the fact that the blade lift is more influenced by the environmental conditions. Also, the mating of the blade with the nacelle hub is a complex operation which can take up more time. The yoke lift has by far the most spreading and highest exposure time. This is due to that for blade lifts sometimes the operator chooses to wait for calmer weather before picking up the next blade. However, the yoke is not lowered on deck between each blade lift. From the time-traces, in appendix B, it can be seen that generally when the yoke is in the hook, it is hanging above the blade rack waiting. Using a confidence interval, a maximum exposure time can be defined for each lifting operation. To quantify the influence of the confidence interval, three different values will be looked at (90%, 95% and 99%). In table H.2, the exposure time is shown for each lifting operation. Depending on the type of lift, the influence of the different confidence intervals, varies. For example, the exposure time of the yoke varies more than two hours between the different confidence intervals. The reason for this can be seen in figure H.6b, it can be remarked that the measured exposure times vary a lot and there are a few extreme outliers. Next to that, for higher confidence intervals, more data is required to get an accurate confidence interval.

For the exposure time used for the time-domain simulations, a 90% confidence interval is chosen. This is common practice in the offshore industry.

4.3.3. Loads in hook

Now that the exposure time of each lift is determined, the load in hook of each lift needs to be specified. The loads lifted by the crane during a wind turbine installation campaign are listed in table 4.1. Each component of wind turbine has a different mass, in [19] the most actual prediction of the mass of each component for a 20 MW wind turbine is found. The mass of each component can change, as no 20 MW wind turbine has been built yet, so current preliminary designs might not yet be fully optimized. Next to the different wind turbine components, the tool to install the blade is also considered, as its mass is large and has a long exposure time.

Table 4.1: Mass of the different components of the wind turbine and tool

Component	Mass [ton]
Tower	2000
Nacelle	1200
Blade	108
Blade tool (Yoke)	200

4.3.4. Chosen crane configurations

For the input of the model, relevant crane configurations need to be chosen. For this, the measurement data described in section 4.3.1 is used. The data used to make the radar plots shown in appendix B is used to define the luffing and slewing angles of the different lifts. The slewing angle for each lifting operation has a starting and ending angle. Because it is unwanted to set constraints on the operation of the crane operator and limit the time the crane can stay at a specific angle during slewing, all slewing angles need to be considered that occur during each lift. This means that at each slewing angle of the lift, the crane should be able to remain the full exposure time of the lift. In this research, the slewing angle will be taken to be perpendicular to the wave heading, as the crane dynamic response is expected

to be the most significant.

In table 4.2 an overview is given, 6 cases have been chosen. The first four configurations describe each lift type (tower, nacelle, blade and yoke lift). The last two configurations describe the crane waiting with no load in hook and when the boom is luffing. It was found in the measured data that the operator, in some configurations, lowered the boom to a luffing angle of 35 degree to wait for more optimal environmental conditions. The load in hook for each case comes from table 4.1 and the exposure time, from table H.2.

Table 4.2: Overview of the chosen crane configurations

Configuration number	1	2	3	4	5	6
Configuration name	Nacelle	Tower	Blade	Yoke	Luffing 35 degree	Waiting
Luffing angle [deg]	75	73	77	77	35	80
Slewing angle, start [deg]	35	55	155	285	30	90
Slewing angle, end [deg]	-235	-235	285	155	30	-285
load in hook [ton]	1200	2000	308	200	100	100
Exposure time [min]	-	-	-	-	-	-
Sling length [m]	30-170	135	30-160	30-160	15	30-180

The sling length is the distance from the crane tip to the COG of the load and has been calculated using the wind turbine dimensions mentioned in [19]. As mentioned in section 3.3.2, the simplification of the sling configuration is considered in the chosen sling length for the different crane configurations When a range of sling length is given, it means that the load is picked up from the jack-up deck and then lifted to the required height for installation. This is, for example, for the nacelle and blades, the nacelle needs to be lifted on top of the tower and the blades need to be connected to the hub which is part of the nacelle. In the case of a tower lift, the sling length remains almost the same, so the average sling length is taken. For the nacelle and blade lift, the minimum and maximum sling length will be investigated. For cases five and six, a conservative exposure time is chosen. From the measurement data, it is not possible to retrieve an accurate estimate of the exposure time when the crane is waiting and luffing. This is because these configurations are used to wait for environmental conditions in which the installation lifts can be performed. So, it is decided to simulate a complete sea-state of three-hour for these two configurations.

5

Description of the jack-up and crane models

As described in section 2.7, it is found that currently the best available method to do time-domain simulation of the dynamic response due to waves of a jack-up and crane for offshore wind turbine installation, is to separate the model in two parts. One part consists of the jack-up and the other of the crane. The separately simulated jack-up motions are used as input for the crane model. In this chapter, the three following items will be discussed:

1. Jack-up model in SIMSEP
2. Crane model in NX-motion
3. Maximum crane capacity definition

Two different time-domain simulation software programs are used to model the dynamics of the jack-up and the crane. In section 5.1, the software used to simulate the jack-up dynamic response is described and in section 5.2, the software used to simulate the crane dynamic response is described. At last, the maximum crane capacity is defined. Different methods and current practice are explained, and the incorporation of the dynamic component is described.

5.1. Jack-up model in SIMSEP

For the simulation of the jack-up dynamic response to waves, GustoMSC's jack-up time-domain analysis program SIMSEP v5.61 is used. In SIMSEP the jack-up structure is modelled as a 3-D finite element model. The legs are represented as a stick model with along the leg length mass lump nodes, [7]. These stick models of the legs are interconnected using a superelement. This superelement can be seen as the hull of the jack-up. In figure 5.1, the jack-up model in SIMSEP can be seen.

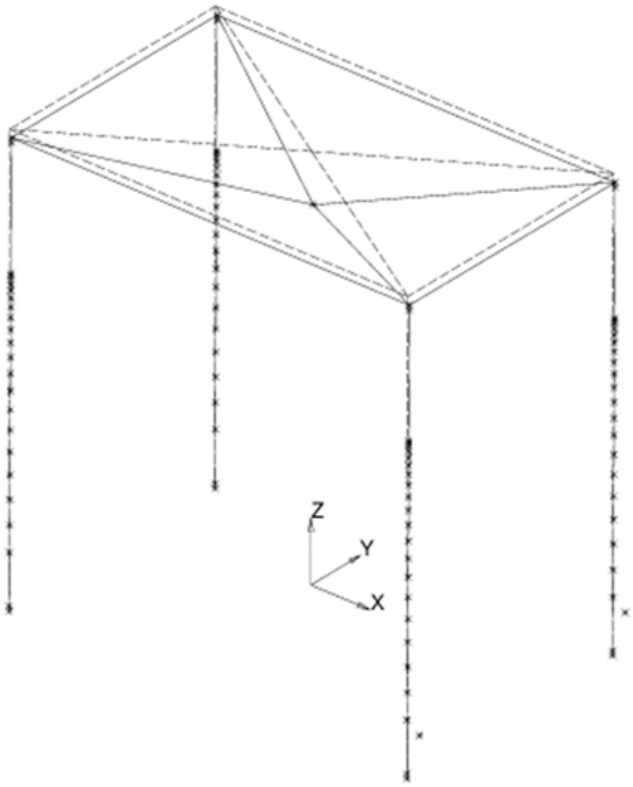

Figure 5.1: Jack-up model in SIMSEP

In the figure, the mass lump nodes of the leg mass can be seen (the crosses). The crane mass is considered as a rigid mass connected to the hull, so the crane dynamics are not considered when simulating the wave induced jack-up response. As mentioned earlier, the jack-up and crane are modelled in two separate models. In the figure, the location of the crane can be seen, the cross represents the crane mass on the deck at the crane location.

The leg-load due to the wave force is calculated using the Morison equation, for more explanation on how this load is calculated, see section 2.2.1. The distributed wave load is calculated for the instantaneous submerged leg length. This distributed wave load is then decomposed into nodal forces and applied on the nodes of the SIMSEP model, see figure 5.1, where the nodes on the legs can be seen. To take the variable leg submergence into account, wave stretching using Wheeler-stretching is applied. SIMSEP takes into account non-linearities of the wave load, the drag coefficient. However, because only small wave heights are considered in this research, only inertia loads are present, which are linear.

The interactions between the leg and hull are modelled as rotational springs, more information is given in section 2.6. In these rotational springs, non-linearities occur, but the wave loads remain small and it can be assumed that only linearities occur. The $p - \Delta$ effect and leg inclination are other non-linearities that can occur in the jack-up dynamics. Because the wave loads remain small, only linear effects are considered. The leg-soil interaction is accounted for using the method described in section 2.5. The soil damping is not explicitly modelled in SIMSEP. To account for soil damping, 5% of the global damping is taken to catch all possible damping in the jack-up. The different parameters, k_h, k_v and k_r, that describe soil stiffness, are retrieved from [1]

To generate the required sea-state for the time-domain simulations,$H_s - T_p$ combinations are used. In section 4.2, the different $H_s - T_z$ combinations, used as input for SIMSEP, are shown. As mentioned, these are first converted to $H_s - T_p$ combinations. The output of SIMSEP are time-traces of the surge, sway and yaw motion of the jack-up at the location of the crane pedestal. These time-traces will be used as input for the crane model. At last, to remove transients in the jack-up time-domain simulation, a ramp-up time, of the input waves, of five times the input T_p is used.

5.2. Crane model in NX-motion

The simulation software used for the crane model is Siemens NX, using subpackage NX-motion. This software is used to make time-domain simulation of the crane dynamic response. NX-motion is a rigid body dynamics tool that can be used to simulate the dynamic response of the crane. NX-motion makes it possible to put the stiffness in the nodes, and the mass and mass moment of inertia in the elements. In figure 5.2, the side and front view of the crane model in NX-motion are shown. In the side view, figure 5.2a, each component of the crane is mentioned.

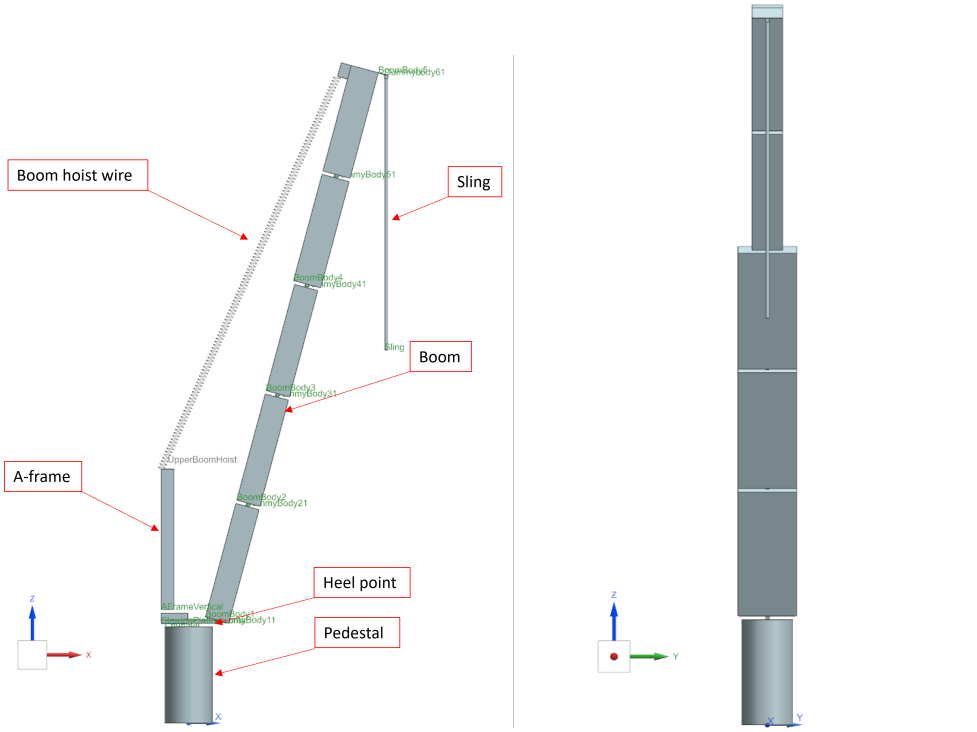

(a) Side-view of the crane model in NX-motion

(b) Front-view of the crane model in NX-motion

Figure 5.2: Side and front view of the crane model in NX-motion

The crane boom is divided into five separate rigid bodies. This is done to limit the number of DoF's and give a more accurate representation of the mass distribution. When looking at the dynamics, if only one body is used to model the crane, the mass will have a much bigger displacement. Using multiple bodies allows for the mass to be distributed along the boom and have more realistic displacements. In figure 5.3, the effect of dividing the boom into multiple bodies on the distribution of the mass, is shown. On the left, the location of the mass is shown when only one body is used and on the right when five bodies are used (the bodies are represented by the dashed lines). It can be seen that the mass points when using five bodies remain closer to the crane boom (represented by the solid line).

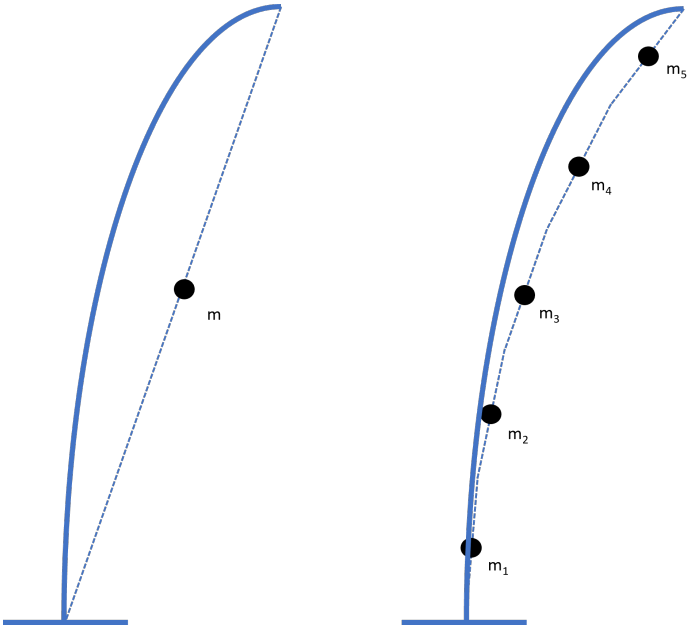

Figure 5.3: Effect of dividing the boom into multiple bodies on the distribution of the boom mass, out-of-plane vieuw

Each body is given mass and mass moment of inertia, for this the structural steel weight of the crane is taken. To account for the crane components that are not structural steel but are also present, like walkways, 10% contingency is added to the structural steel weight. The inertia moment is linearly related to the crane mass, and therefore there is also 10% inertia contingency. These 5 bodies, are connected to each other by rotational springs and dashpots, which model the boom stiffness and allow for rotation in- and out-of-plane.

To determine the stiffness of the rotational springs in between each body, a pushover analysis is performed on a finite element model of the crane, see section 5.2.1 for the explanation. The damping of these rotational springs also needs to be added, this done by doing a decay test, see section 5.2.2.

The A-frame is modelled as two bodies to allow translation in x- and z-direction. To not add any inertial forces to the model and to only contribute to the overall flexibility of the model, very little mass is assigned to these bodies. The boom hoist wire is modelled as a spring, as investigated in section 3.3.1, the mass of the boom hoist wire can be neglected, so representing the boom hoist wire as a spring is an acceptable assumption. The sling is connected to the crane tip by a dummy-body, to allow rotation. The sling is modelled as a rigid body of which the length can be adjusted to the load case. At the lower end of the sling a mass point is inserted representing the load in hook. The length of the rigid body modelling the sling is equal to the distance between the crane tip and the COG of the load that is lifted. At the bottom of the crane pedestal, a driver is placed to insert the motions of the jack-up in x- and y-direction and the rotation around the z-axis. In this case, the inserted motions will be the jack-up motions simulated by SIMSEP.

Because the crane is a low damped structure, there is a possibility that transients occur in the time-domain simulations. These transients affect the result and are unwanted. Therefore, to remove these possible transients and get the required steady-state, a ramp-up of the input motions is required. This is done by adding a ramp-up time to the SIMSEP jack-up motion input. Compared to the jack-up, the crane is a low damped structure therefore more ramp-up time is required than for the jack-up. The ramp-up time for the crane in NX-motion is set to 1000 seconds.

5.2.1. Crane stiffness

To determine the stiffness of the crane boom, a pushover analysis is performed on the NX-motion model. For this, the model needs to be modified for the in-plane and out-of-plane analysis. The out-of-plane pushover analysis is performed by clamping the model at the boom hinge and applying a force to the crane tip, see figure 5.4. Where F is the applied force and U_i are the joints, with i going from one to four. The stiffness due to the spring representing the boom hoist wire rope is neglected in this analysis.

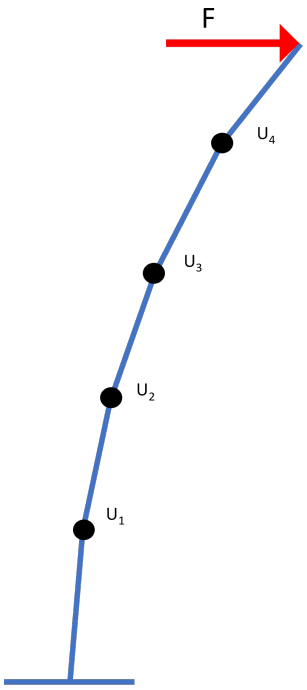

Figure 5.4: Out-of-plane pushover analysis sketch

The displacement of each joint can be retrieved from the NX-motion model. From the displacement the moment and rotation at each joint can be calculated, from which the rotational stiffness at each hinge can be derived, see equation (5.1).

$$k_r = \frac{M}{\theta} \tag{5.1}$$

Where:

k_r = Rotation stiffness
M = Moment in the hinge
θ = Body rotation

The in-plane stiffness of the crane boom, is determined by simply supporting both ends of the crane boom and applying a force at the two middle joints, see figure 5.5. The same method then applies as used for the out-of-plane stiffness analysis.

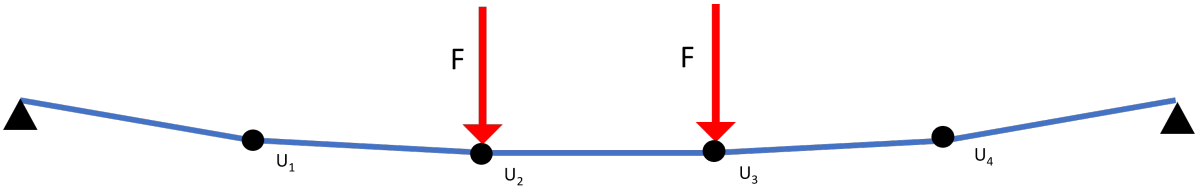

Figure 5.5: In-plane pushover analysis sketch

5.2.2. Crane damping

The required damping that is necessary to model the crane properties needs to be calculated. To determine the required damping in the model at each dashpot, a decay test is performed. Thereafter, the mentioned displacement is applied, the boom is released and the decaying of the displacement is analysed. The damping value is increased, using an iterative procedure, until the first out-of-plane mode is found. This is when the displacement is exponentially decaying. The first out-of-plane mode damping is between 0.5 to 1% of the critical damping. In figure 5.6, the time-trace of the out-of-plane motion of the crane tip during a decay test is plotted.

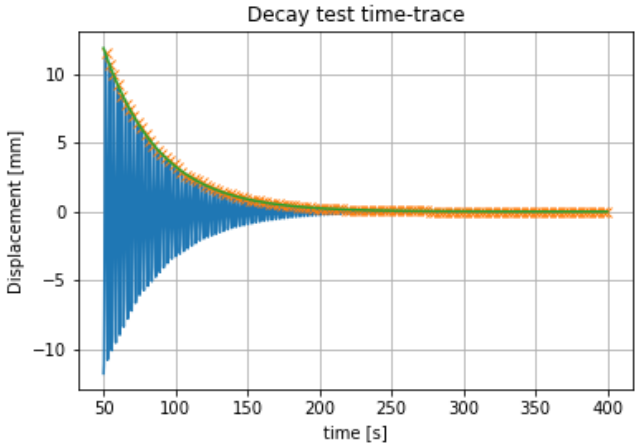

Figure 5.6: Plot of the displacement of the crane during a decay test

To determine the percentage of damping, the peaks of the decay test are fitted. Applying the described method to the selected crane, the required damping is calculated to be 0.84% of the critical damping.

5.3. Maximum crane capacity definition

To be able to calculate the annual probability of failure, a limit needs to be defined for the crane capacity. This research focusses on the dynamic response of the crane. Currently, no rules, from classification societies, are available to define the limiting crane capacity due to the load caused by the dynamic response of the crane to wave induced excitations. For this research, the best available method is researched. Below, multiple different failure mechanisms will be discussed and the most relevant one will be chosen. Multiple failure mechanisms are present that could be induced by the dynamic response of the crane. The best available method is dependent on the main dynamic mechanism. Because the crane consists of multiple braces and the crane boom width changes over the length, the moment distribution along the crane boom is not constant. Depending on the load in the crane, the maximum load can occur at a different place, allowing for different failure mechanisms.

If, for example, a high load in the crane tip occurs, due to for example high sling dynamics, the moment distribution along the boom is different than when the boom vibrates a lot. Another failure mechanism is the load-boom clearance, it is unacceptable that the load in hook comes into contact with the crane boom due to excessive swinging of the load in hook. This will result in damage to the load in hook and to the boom, which can have a structural impact on both. This should be avoided at all cost. This failure mechanism is only relevant if the dynamic response of the sling is large.

For the design of cranes, the maximum side lead angle when picking up a load is used to define the maximum capacity. When picking up a load, it is difficult for the operator to put the crane tip exactly above the load. Therefore, a maximum side lead angle is defined that the crane should be able to support. This maximum side lead angle can be used to calculate the maximum allowed moment, due to static loads, at a specific location in the crane.

The maximum crane capacity (MCC) is taken as the maximum allowable moment in the heel point of the crane based on a defined side lead. This is seen as the best available method, as it is already used in crane design for static load cases. Furthermore, from the NX-motion model of the crane, the moment can be simulated at any given point in the crane. The location of the heel point can be seen in figure 5.2a.

As mentioned, current practice is to look at the maximum side-lead angle of the load in hook to calculate the MCC. This is done for a static side-lead angle, so no dynamic response of the crane or the sling is considered. In this thesis, the failure of the crane due to the dynamic response is investigated, so the allowable moment induced by this dynamic response needs to be defined. The definition of the side-lead angle (θ) can be seen in figure 5.7.

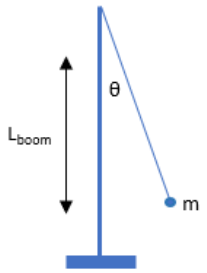

Figure 5.7: Definition for the MCC calculation

From the DNV Lifting Appliances, [26], a maximum allowable static side-lead angle of the load (out-of-plane) regarding the boom is given. This angle is equal to two degrees, this means that the load can be a maximum of two degrees out-of-plane regarding the crane boom. These two degrees account for static loads, like when picking up a load from the deck. However, these two degrees do not explicitly account for the crane dynamic response, which is investigated in this thesis. It is therefore necessary to define how this dynamic response needs to be incorporated into the MCC. It needs to be determined wherever this takes up a part of the allowed two degrees, thus reducing the remaining capacity for the other effects mentioned above, or that the allowed side-lead angle for dynamic loads need to come on top of these two degrees.

The latter is chosen, because when picking up a load, there is no dynamics in the sling and when the load has been picked up the sling can undergo dynamics. In this thesis, it is decided that the maximum side-lead angle due to crane dynamics is equal to 0.5 degrees. The effect of the deadweight of the crane and the dynamic response due to wind loads are implicitly accounted for in this chosen side-lead angle. This extra allowed side-lead angle comes on top of the previously allowed two degrees side-lead.

Below, the equation is given to calculate the maximum crane capacity at the heel point due to the chosen allowable static side lead angle.

$$MCC = m_{max} \cdot L_{boom} \cdot \theta \tag{5.2}$$

Where:

θ	=	Maximum allowable side-lead angle [degree]
L_{boom}	=	Length of crane boom [m]
MCC	=	Maximum crane capacity [MNm]
m_{max}	=	Maximum load in hook [kg]

In the case of the chosen crane, with a boom length of 167 meters, a maximum lifting capacity of 2000 tons and a maximum allowable side-lead of 0.5 degrees, the maximum crane capacity is equal to 28.59 MNm. This signifies that the maximum moment in the hinge, induced by the crane dynamics, cannot exceed the above calculated maximum moment. Otherwise, the reserved capacity for crane dynamics, is exceeded.

The chosen method above has multiple limitations. The main limitation is that the chosen allowable side lead angle for the dynamic response of the crane is based on an assumption. No crane strength calculations have been performed to support this side lead angle. Furthermore, the static side lead angle is chosen to be next to the required two degree side lead angle, required for picking up loads from the deck. Likewise, it is possible that this should be subtracted from this two degree side lead angle, if they both occur at the same time.

6

Methodology to calculate the annual probability of failure

Now that the SIMSEP and NX-motion models have been described in chapter 5 and the required input for the models has been described in chapter 4, a method to calculate the annual probability of failure (APF) is developed. First, the reason a methodology is required for the calculation of the annual probability of failure of the crane is explained. For this, the maximum moment is calculated, it is found that multiple seeds are required to get a converging results. From these multiple seeds, the statistical description of the crane dynamics is investigated.

Because multiple seeds are required for convergence of the result, a methodology is developed to limit the required number of time-domain simulations to calculate the APF. This methodology is based on a spectral analysis. The different aspects of this spectral analysis are explained. This consists of the different steps and the selection parameters that are used. These parameters are also checked, for example spectra. The encountered numeric issue are discussed and solved. The devised spectral analysis is then applied to a reference configuration and checked. After the validation of the spectral analysis, the different steps of this analysis are summarized. To conclude, the steps to calculate the APF of the crane are shown. The different steps to consider the different probabilities of the cases, are covered. The items mentioned above are shown in figure 6.1.

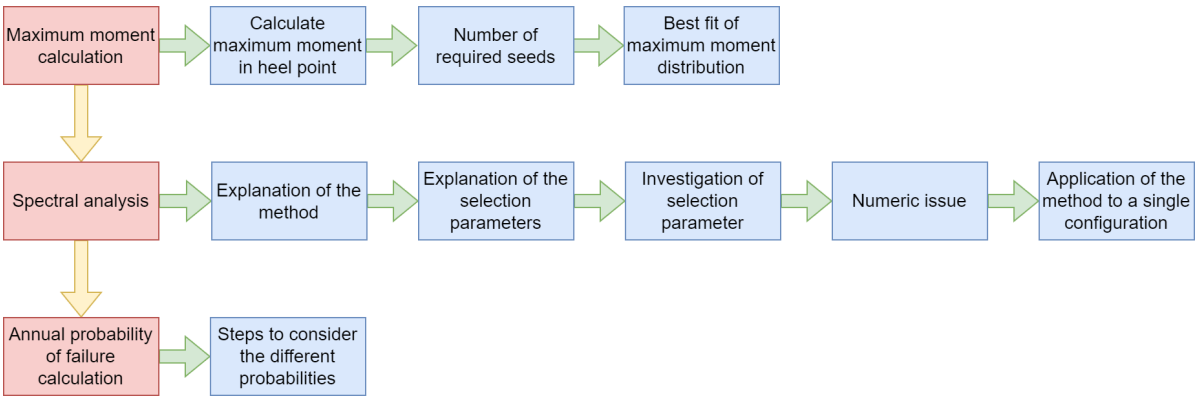

Figure 6.1: Overview of the items discussed in the methodology

6.1. Maximum moment calculation

To be able to calculate the APF, the statistical properties of the crane dynamics are investigated. To start, the statistics of the maximum moment are investigated. For this, the moment in the heel point due to the wave induced excitations needs to be calculated. Below, the different steps are explained to go from a time-domain simulation of the moment in the heel point to a maximum moment distribution of multiple sea-states.

6.1.1. Method to calculate the maximum moment

The different jack-up and crane configurations, chosen in chapter 4, are used as input for the different time-domain simulation models described in chapter 5. Using SIMSEP, the dynamic response of the jack-up due to the wave induced excitation can be simulated in the time-domain, for a specific $H_s - T_p$ combination. The motions of the jack-up are simulated at the crane pedestal base. These three-hour time-domain simulations, of the dynamics of the jack-up, can be used as input for the NX-motion model. In NX-motion, the time-domain simulations, of the dynamic response of the crane, are performed. From this, a time trace of the bending moment at the heel point can be retrieved. The location of the heel point can be seen in figure 5.2. From each NX-motion time-domain simulation, the maximum moment is retrieved. Because waves have a random nature, see section 4.1, it is not possible to only use one sea-state to get an accurate maximum moment. Each sea-state has a random phase, resulting in a different outcome. To account for this, multiple time-domain simulations of the crane dynamics with random sea-states are required. From these multiple time-domain simulations, the distribution of the maximum moment of each simulated sea-state can be made, see figure 6.2.

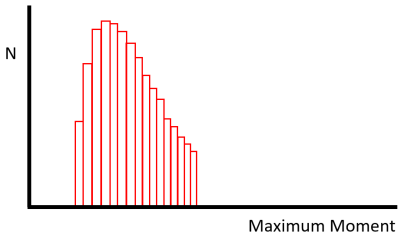

Figure 6.2: Distribution of the maximum moment of each sea-states, example

To evaluate the number of required time-domain simulation (number of seeds), the convergence of the distribution of the maximum moment of each seed, needs to be investigated, this is done in section 6.1.2.

6.1.2. Number of required seeds

To investigate the number of required simulations to get a converged distribution of the maximum moment of each seed, a convergence test is performed on the required number of seeds. For this, one case is chosen and one H_s-T_p combination for the time-domain simulations. Five different seed sizes are investigated. In figure H.12, the distributions of the maximum moment for varying seed sizes are shown.

In table 6.1, the coefficient of determination (R^2) value, mean and 90%, 95% and 99% confidence intervals of the distribution of the maximum moment, are shown for different seed sizes.

Table 6.1: R^2, mean and 90%, 95% and 99% confidence intervals of the maximum moment distribution for different seed sizes

Seed size [-]	40	60	80	100	120
R^2 [-]	0.441	0.460	0.499	0.501	0.502

In figure H.12, it can be seen that the distribution of the maximum moment of each seed, for a seed size of 100 and 120 seeds, are similar. For smaller seed sizes, the distributions are different. Therefore, it can be said that for a seed size of 100 seeds, convergence has occurred. Looking at 6.1, it can be seen that the R^2 value convergences for a seed size of 100 seeds. Furthermore, increasing the seed size results in a convergence of the different maximum moment confidence intervals. The confidence interval bounds are more accurate. The average of the maximum moment remains at the same place, but the extremes get more accurately described by the fit with a higher number of seeds. It is chosen to use a seed size of 100, as the confidence intervals are seen to converge for this value. For a confidence interval of 99% the required seed sizes needs to be higher to have convergence. However, for the future steps, only a confidence interval of 90% is used. Using a 90% confidence interval is common practice in the offshore industry. The chosen seed size is based on one JU and crane configuration, and sea-state, it is assumed that the same applies for other configurations.

6.1.3. Best fit of maximum moment distribution

The fit shown above has been made of the distribution of the maximum moment of each seed, to check for the required seed size. This fit is required to get a probability description of the distribution, in figure 6.3, an example fit is shown plotted over the example distribution shown in figure 6.2.

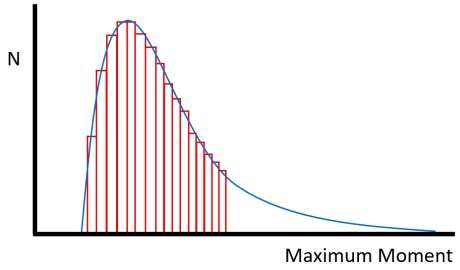

Figure 6.3: Moment distribution example with fit

Using the fit, it is possible to calculate the confidence interval of the distribution. For example, in figure 6.4, the 90% confidence interval of the distribution is shown.

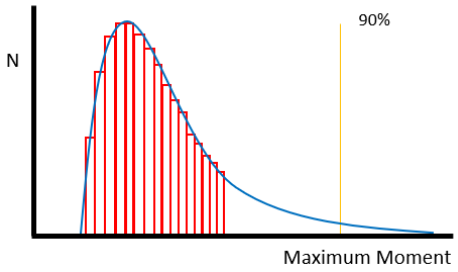

Figure 6.4: Moment distribution example with fit and confidence interval

To find which type of probability distribution describes the distribution of maximum moment of each seed, in the most accurate manner, the following steps are performed. To start, multiple different types of probability distributions are fitted to the data for a seed size of 100 seeds, and the R^2 is calculated. The coefficient of determination gives an order of variation between the histogram of the calculated maximum moment and the fitted probability distribution. In appendix C, the different types of distributions fitted over the calculated maximum moment distribution can be seen.

The best fit of the data is found for an Exponentiated Weibull distribution, see section 7.1.1 for the results. Below, the probability and cumulative density function equations are shown, respectively, [17].

$$f(x;k,\lambda;\alpha) = \alpha\frac{k}{\lambda}\left[\frac{x}{\lambda}\right]^{k-1}\left[1-e^{-(x/\lambda)^k}\right]^{\alpha-1}e^{-(x/\lambda)^k} \tag{6.1}$$

$$F(x;k,\lambda;\alpha) = \left[1-e^{-(x/\lambda)^k}\right]^{\alpha} \tag{6.2}$$

Where:

f	=	Probability density function
F	=	Cumulative density function
k	=	First shape parameter
α	=	Second shape parameter
λ	=	Scale parameter
x	=	Maximum moment

6.1.4. Conclusion of maximum moment calculation

Now that the required number of seeds and the statistical fit of the distribution of the maximum moment of each seed are known, the APF can be calculated. However, if for each case with a different crane configuration, jack-up configuration and sea-state, 100 time-domain simulations are required. This results in 3,240 cases and thus 324,000 different time-domain simulations. Performing all these time-domain simulations is unwanted. In the following section, a methodology is set-up, to limit the required number of time-domain simulations.

6.2. Spectral analysis

It is found above that to get the maximum moment in the crane, 100 seeds are required. Doing this for each different case is unwanted. A method is researched to limit the number of required time-domain simulations and being able to calculate the maximum moment of 100 seeds based on one time-domain simulation. This is done by looking at the frequency domain spectrum of the time-domain simulations.

In figure 6.5, a typical frequency domain spectrum is shown where all three dynamic components (jack-up, crane and sling) can be seen. Around an angular frequency of 0.5 rad/s the sling peak can be found, around 0.9 rad/s the jack-up peak and around 2.3 rad/s the crane peak. The location of each peak is dependent on the jack-up, crane and sling configuration. The sling fundamental natural frequency changes due to the varying sling length of each configuration. The jack-up fundamental natural frequency is dependent on the leg length. The crane fundamental natural frequency is dependent on the crane boom length.

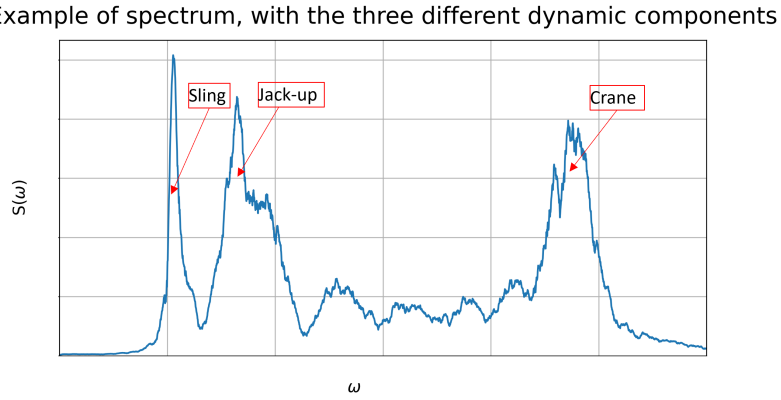

Figure 6.5: Definition of the peaks in an example spectrum

6.2.1. Spectral analysis method

To narrow down the number of required time-domain simulations, a spectral analysis is performed. For this, the frequency domain spectra of the cases are investigated. Based on the frequency domain spectrum, the significant value of the frequency domain spectrum can be calculated. From this, the ratio between the significant value and the maximum moment can be calculated. This ratio is expected to be the same when two spectra have the same statistics. Two cases have the same statistics when the spectra of these cases have the energy at the same location. The location of the energy gives a measure of the number of peaks in the time-domain. The higher the number of peaks, the higher the probability of an extreme.

To calculate the amount and location of the energy in the spectrum, a spectral analysis is performed. This spectral analysis consists of calculating multiple parameters of the frequency domain spectrum, these parameters are described in see section 6.2.2. To get a feeling of the statistical properties of the different jack-up and crane configurations without running multiple seeds, a spectral analysis of all the different cases chosen in section 4.2 and 4.3.4 is performed. This is done by performing a Fast Fourier Transformation (FFT) on the output time-traces of the crane moment in the heel point, simulated using NX-motion. Using this, the frequency domain spectrum can be derived for the different cases. All the different wave heading and $H_s - T_p$ combinations are investigated. From the frequency domain spectra, cases with similar statistics can be identified. Using this, cases with the same statistics can be grouped.

When two cases have the same statistics, the normalized distributions of the maximum moment of each seed, are also the same. Now, only one case of each group is required to be simulated, for 100 seeds, to get the distribution of the maximum moment of each seed. After normalizing the found distribution, the distribution is scaled using the maximum moment of the cases where only the spectral analysis is performed. To get this maximum moment, the ratio between the significant value and the maximum moment is investigated (this ratio is named ratio β), see equation (6.3).

$$M_{max} = \beta \cdot \sigma \tag{6.3}$$

Where:

M_{max} = Maximum moment of the distribution
σ = Significant value of the spectrum

It is investigated if ratio β can be calculated based on parameters of the frequency domain spectrum of each case. It is expected that there is a relation between the spectrum and ratio β. Using the found relation, an equation is derived, with which ratio β can be calculated for each case. Using ratio β, the normalized distribution of the maximum moment can be scaled. Using the found distribution of maximum moment of each seed, the probability of exceeding the maximum moment allowable moment in the heel point can be calculated. In figure 6.6, the steps described above are shown in a diagram.

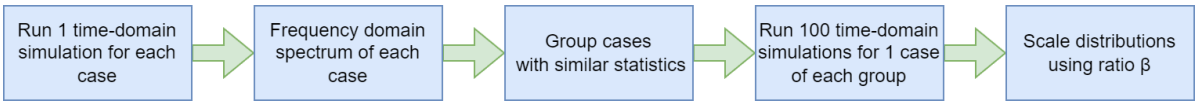

Figure 6.6: Steps of the spectral analysis

The described steps above are checked for a reference configuration, in section 6.2.5. For one configuration, the different $H_s - T_p$ combinations are run for the selected seed size. The spectrum of each case is investigated and two similar spectra are selected to validate the assumption that the statistics are the same. For this, the distributions are normalized for a better comparison. The ratio between the average significant value of the 100 seeds and the maximum moment (ratio β) is calculated. It is expected that ratio β is the same for the two selected cases.

Subsequently, the assumption is validated, ratio β based on 100 seeds is calculated for each case of the reference configuration and the relation between the spectrum and ratio β is investigated. From this, an equation to calculate ratio β based on a frequency domain spectrum is derived. At last, a summary of the steps of the spectral analysis is given.

6.2.2. Selection parameters

To be able to combine cases with similar statistics, a method is developed to get an insight of the statistics of each configuration. For this, the spectra of each configuration for multiple $H_s - T_p$ combinations are calculated. The frequency domain spectrum is calculated using a time-domain simulation of the maximum moment in the heel point. Using the frequency domain spectrum, the spectral density of the different peaks can be defined. Therefore, the spectral energy of the crane, jack-up and sling component can be identified. In figure 6.7, the definition of the spectral density is shown. Where, $\Delta\omega$ is the frequency interval and $S(\omega)$ is the energy spectrum.

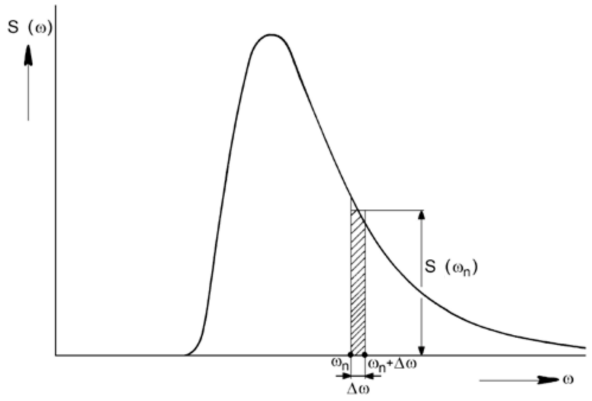

Figure 6.7: Definition of spectral density, [11]

For wave statistics, the wave energy spectra are used to derive the statistics of a sea-state. It is known that there is a relation between the wave height and period and the moments of the area under the spectrum, [11]. It is expected that the same applies for the crane statistics, that from the different nth-order moments, something can be said about the amplitude and return period of the moment in the crane. Therefore, the nth-order moments of the peaks of the different components of the spectra, mentioned in section 6.2, give an approximation of the dynamics of each case. The nth-order moments are calculated as following:

$$m_n = \int_0^\infty \omega^n \cdot S(\omega)\, d\omega \tag{6.4}$$

Where:

m_n	=	nth-order moment
ω	=	Frequency
$S(\omega)$	=	Spectral density
n	=	Order; 0, 1 and 2

The zeroth-order moment is the area under the curve. Therefore, the amount of energy of the component can be found using this value. The first-order moment usually gives the static moment of the component. So, the higher the frequency of the peak, the higher the first-order moment is. The second-order moment is the moment of inertia, the higher frequency the energy is located, the higher the second order moment is. Using the second moment, the mean zero-crossing period can be calculated, see equation (6.8). From the different order moments described above, using equation (6.4), the characteristic periods can be derived:

$$m_1 = \omega_1 \cdot m_0 \tag{6.5}$$

$$m_2 = \omega_2^2 \cdot m_0 \tag{6.6}$$

Where:

ω_1	=	Spectral centroid
ω_2	=	Spectral radius of inertia

From the spectral centroid, the mean centroid can be calculated. The same applies for the spectral radius of inertia, from which the mean zero-crossing period can be calculated:

$$T_1 = 2\pi \cdot \frac{m_0}{m_1} \tag{6.7}$$

$$T_2 = 2\pi \cdot \sqrt{\frac{m_0}{m_2}} \tag{6.8}$$

Where:

T_1 = Mean centroid period
T_2 = Mean zero-crossing period

The mean centroid period is the average period of the spectra without accounting for the amplitude of the different peaks in the spectra. The mean zero-crossing period gives a measure of the number of peaks in a time-trace. The smaller the mean zero-crossing period, the more peaks there are in the same time-interval and the higher the probability that an extreme occurs. The mean zero-crossing period is also denoted by T_z. To get a feeling on how these parameters are affected by different types of spectra, some generic spectra are investigated in section 6.2.3.

6.2.3. Investigation into selection parameter

The amplitude of the different moments and the ratio's of the-nth order moments between different components are investigated. To start, an investigation is done with generic spectra, to see what the influence of different spectra is, on the selected parameters. Three different spectra are looked at. Below each example spectra is described, shown in a figure and the parameters, described previously, are listed and reviewed. Example one has two spectra with different amplitudes, but at the same location. The two spectra can be seen in figure 6.8.

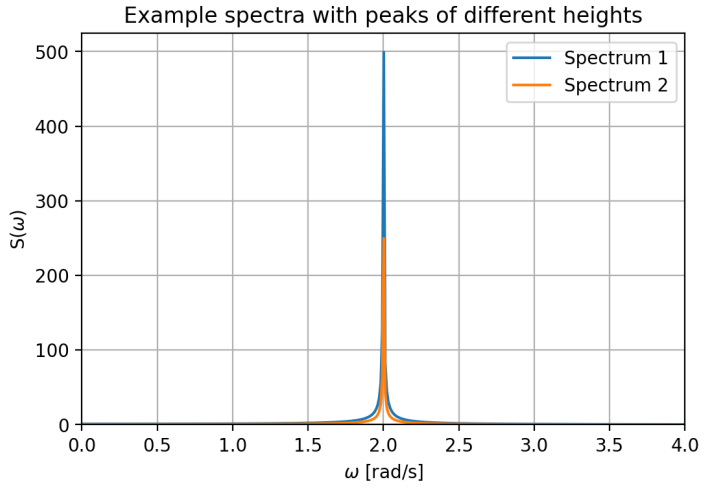

Figure 6.8: Two spectra with different amplitudes

In table 6.2, the ratio between the two spectra of the zeroth, first and second-order moments are shown. The second spectrum is half the height of the first spectrum. The nth-order moments of the second spectrum are all half the size compared to the first one. The energy in the second spectrum is half of the first spectrum. The mean centroid and mean zero-crossing are nevertheless the same. This means that the amplitude of the peak has no influence on the different periods.

Table 6.2: Ratios for case 1

Ratio m_0 [-]	Ratio m_1 [-]	Ratio m_2 [-]	Ratio T_1 [-]	Ratio T_2 [-]
0.5	0.5	0.5	1.0	1.0

Example two has two spectra with different scales, but with the same spectral density. The two spectra can be seen in figure 6.9.

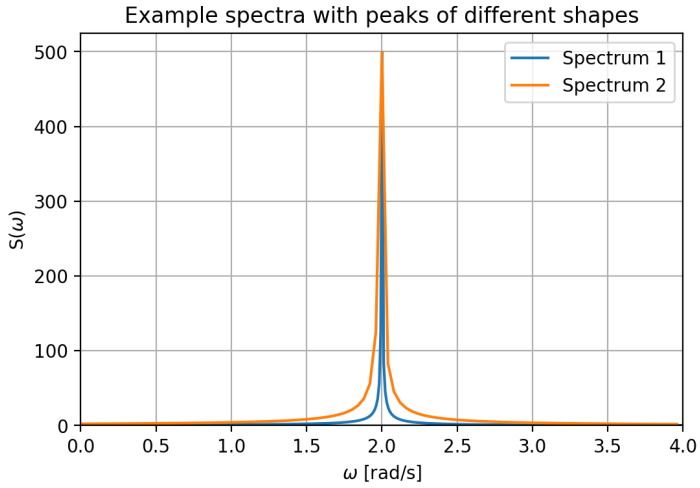

Figure 6.9: Two spectra with different scales

In table 6.3, the results of example two can be seen. The zeroth-order moment is three time bigger for the second spectrum. This is because the peaks have the same height, but the second spectrum is wider. It can be remarked that the difference decreases for the higher order moments. The second spectrum has a bit higher mean zero-crossing period. This means that the probability of maximum is higher as there are more zero-crossings. The width of the peak is also relevant for the number of expected zero-crossings.

Table 6.3: Ratios for case 2

Ratio m_0 [-]	Ratio m_1 [-]	Ratio m_2 [-]	Ratio T_1 [-]	Ratio T_2 [-]
3.15	2.98	2.47	1.06	1.13

Example three has two spectra with the same scale, but with different location of the peak. The spectra can be seen in figure 6.10.

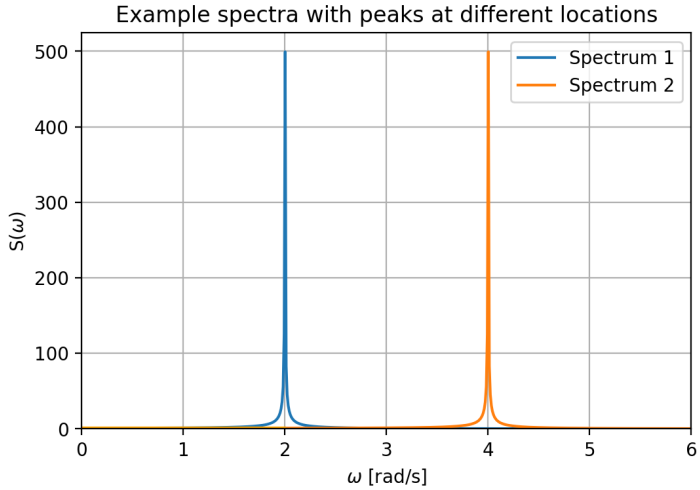

Figure 6.10: Two spectra with different locations

The ratios of the nth-order moments and the mean centroid and mean zero-crossing period between the two distributions are shown in table 6.4. The zeroth-order moment are the same because the

spectra have the same shape. However, because the second spectrum is located at a higher frequency, the first- and second-order moments are bigger for the second spectrum. The first-order moment gives the location of the peak and the second-order moment the number of peaks there are in the time-domain. It can be seen that the second peak has more zero-crossings. This can also be remarked in the mean centroid and mean zero-crossing period. For the second spectrum, the mean zero-crossing period is around two times smaller than of the first spectrum, so it is expected that there are two times more peaks in the second spectrum.

Table 6.4: Ratios for case 3

Ratio m_0 [-]	Ratio m_1 [-]	Ratio m_2 [-]	Ratio T_1 [-]	Ratio T_2 [-]
1.0	1.96	3.31	0.51	0.55

From the three example spectra, it can be concluded that the nth-order moments give a measure of the size and location of the peak. Furthermore, the number of zero-crossings can be found, which gives a measure of how many peaks occur and the probability an extreme can occur.

6.2.4. Numeric issues

While investigating the frequency domain spectra of different configurations, it is noticed that the output spectra have noise, see figure H.13a. To remove this noise, a Savitzky-Golay filter is used to smooth out the spectrum of each simulation. The Savitzky-Golay filter, uses the least square method to fit a polynomial to a predetermined group of data-points to calculate the smoothed value, [16]. The order of the polynomial and the number of data-points are used as input for the filter, next to the to be smoothed data set. A third order polynomial and a window size of 51 data points are used. After using the Savitzky-Golay filter, the output is much smoother and the noise in the output spectrum is removed, see figure H.13. The different components of the spectrum are now much clearly distinguishable. This gives a better visualization of the spectra and the different peaks.

6.2.5. Application to a single configuration

To check if the method described above is applicable, one configuration is chosen to generate results. The selected configuration are investigated for different sea-states (one H_s and multiple T_p). First, the selected configuration is described, next the frequency domain results are shown from which a hypothesis is formulated. The hypothesis is checked and then the results for all the T_p's are looked at. From the found results, ratio β is calculated. Thereafter, it is checked if it is possible to calculate ratio β based on the parameters of the spectra described previously. At last, the sensitivity due to the spread of the significant value is checked.

Selected configuration

The selected configuration is a nacelle lift, with a fully loaded jack-up and water depth of 60 meters. This case is chosen because the sling length can be varied and the load in hook is relatively high. Unlike a tower or blade lift. In the chosen configuration, the sling length is 170 meters, which means that the nacelle is just above the deck of the jack-up. The input sea-state is an H_s of 3 meters and the T_p is varied between 3 and 12 seconds, with a step size of 1 second. The selected case has an exposure time of approximately one-hour, however for this investigation, three-hour time-domain simulations are performed and used for the investigation into ratio β. This is chosen as it adds the possibility to investigate the sensitivity of the exposure time on the ratio β in a later stage. The wave heading is 0 degree, which means that the waves come head-on, on the jack-up. To get maximum crane excitations, the slewing angle is 90 degree, and thus the crane is perpendicular to the wave heading.

Frequency domain analysis

To start, the configuration is investigated in the frequency domain, to get an idea of the expected motions. For this, one time-domain simulation is performed of the jack-up motions for a random sea-state with a selected $H_s - T_p$ combination. The jack-up motions are then used as input for the NX-motion

crane dynamic simulation. Using an FFT, the frequency domain spectrum can be calculated, see figure 6.11. The spectra of the chosen crane configuration can be seen for different T_p. Furthermore, the nth-order moments of the different peaks are shown and the component with the highest nth-order moments is highlighted. The peak, with the highest nth-order moment, is the dominant peak. Using this, it can be investigated if there is a difference, between the dominant peak based on a visual analysis and based on the calculated nth-order moment.

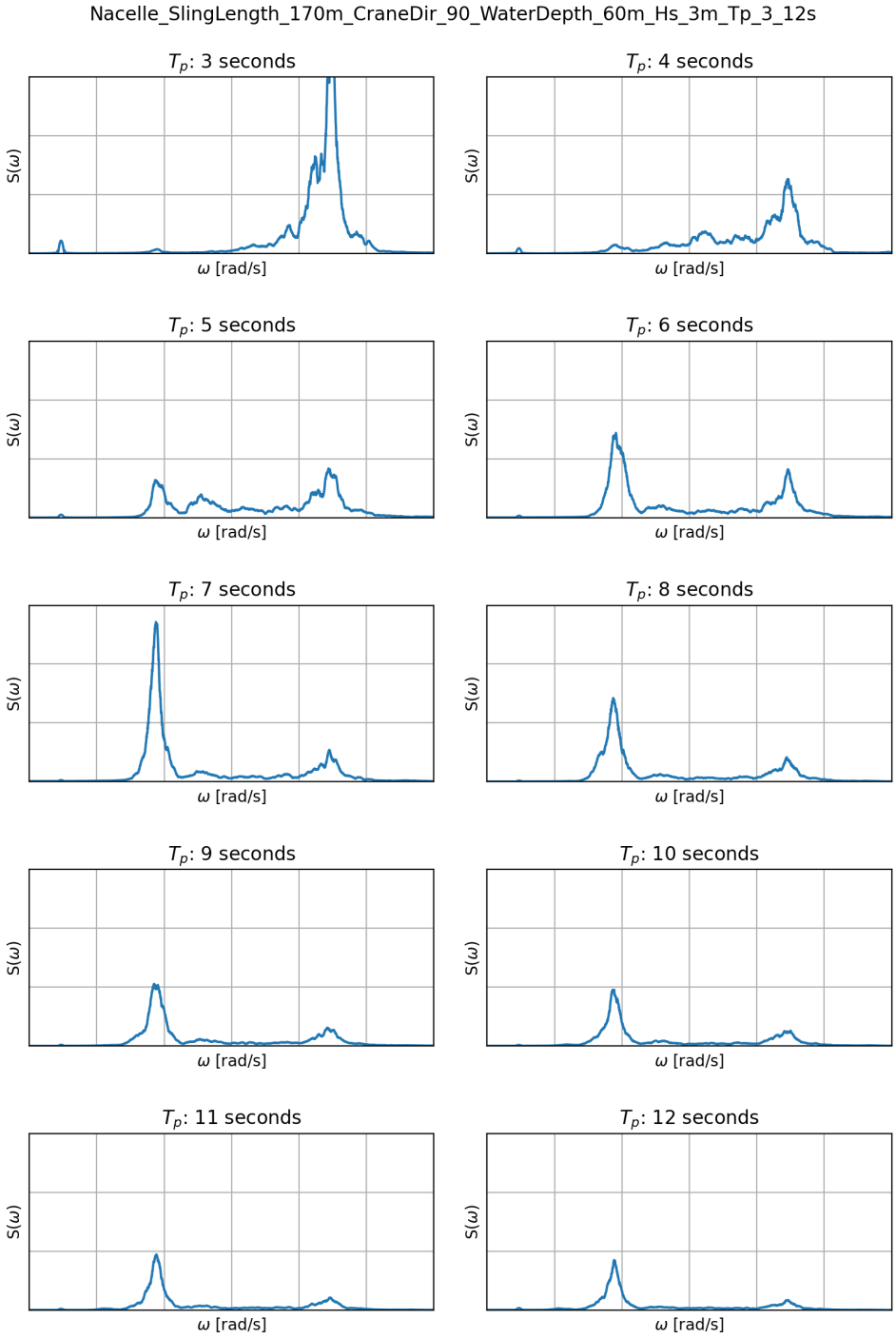

Figure 6.11: Spectra of the selected configuration for different wave peak periods

The spectrum with a T_p of 3 seconds is dominated by the crane dynamics and has the highest peak of all cases. The fundamental natural period of the crane, in this case, is the closest to the excitation

period of the waves. The spectra of T_p of 4 and 5 seconds have a crane component and some spectral energy in between the jack-up and crane peak. For a T_p of 6 seconds, the jack-up peak is more important, but from the nth-order moments it can be remarked that the crane peak is still dominant. The spectrum for a T_p of 7 seconds is also different from the rest, the jack-up peak is the highest. This comes from the fact that the fundamental natural period of jack-up is close to the T_p of 7 seconds. The spectra for a T_p of 8, 9 and 10 seconds have a jack-up and crane peak of similar size. The spectra of 11 and 12 seconds have a high jack-up peak and a small crane peak. Compared to the spectra of 8, 9 and 10 seconds, the crane peak has less influence (lower first order moment). It can be remarked that the sling dynamics are negligible for this configuration. This is, however, expected as the sling is long and has a fundamental natural period far away from the excitation T_p. The fundamental natural period of the sling for this configuration is 26 seconds, which is much higher than the maximum investigated T_p.

Hypothesis

To investigate if combinations with the same spectra have the same ratio between the significant value of the time-domain simulation and the maximum moment, a hypothesis is formulated. It is expected that the ratio between the significant value and a confidence interval is the same for two different cases with similar spectra and statistics. This is checked for the cases with T_p of 8 and 9 seconds.

In figure 6.11, it can be seen that the spectra of the mentioned cases look similar. The mean zero-crossing period of the spectra of the two cases are the same. In table 6.5, the mean zero-crossing period of each component is listed for the cases with T_p of 8 and 9 seconds. The mean zero-crossing periods of the crane and jack-up peaks are similar. The T_z of the sling are different, but as can be seen in figure 6.11, the sling peak is negligible.

Table 6.5: T_z of the crane, jack-up and sling

T_p [s]	$T_{z,crane}$ [s]	$T_{z,jack-up}$ [s]	$T_{z,sling}$ [s]

In table 6.6, the ratio between the crane (C), jack-up and sling (S) zeroth, first- and second-order moments are listed for the cases with a T_p of 8 and 9 seconds. Based on table 6.6, it can be seen that the ratios between the crane, jack-up and sling peak of the nth-order moments are similar. If the calculated ratios are the same for the two selected cases, then the statistics of the cases are similar.

Table 6.6: Ratios between the different order moments of the different peaks

T_p [s]	Ratio $m_{0,C}/m_{0,JU}$ [-]	Ratio $m_{1,C}/m_{1,JU}$ [-]	Ratio $m_{2,C}/m_{2,JU}$ [-]
8	0.44	1.06	2.51
9	0.43	1.03	2.42
T_p [s]	Ratio $m_{0,C}/m_{0,S}$ [-]	Ratio $m_{1,C}/m_{1,S}$ [-]	Ratio $m_{2,C}/m_{2,S}$ [-]
8	16.67	84.69	369.86
9	16.01	70.11	277.73
T_p [s]	Ratio $m_{0,JU}/m_{0,S}$ [-]	Ratio $m_{1,JU}/m_{1,S}$ [-]	Ratio $m_{2,JU}/m_{2,S}$ [-]
8	37.56	80.12	147.24
9	36.92	68.31	114.59

Now that it is found that the two selected cases of the hypothesis have the same nth-order moments ratios, the results of the time-domain simulation are investigated. This is required to check the ratio between the significant value and the maximum moment (ratio β). For this, 100 time-domain simulations are performed in NX-motion. In figure H.7 and H.8, the results can be seen. The normalized PDF of the maximum moment is plotted, the PDFs are normalized around the different confidence intervals (90%, 95% and 99%), so for example, for a confidence interval of 90%, 90% of the distribution is left of 1. The PDFs of the normalized maximum moment for a T_p of 8 and 9 seconds are similar, when increasing the confidence interval, the difference increases, as expected. For a confidence interval of 90%, it can be said that the distributions of the maximum moment of each seed, are similar and therefore the statistics are the same.

In table 6.7, the ratio between the significant value of the time-domain simulation and the maximum moment of the different confidence intervals are shown. The differences between ratio β for a T_p of 8 and 9 seconds are negligible. For a confidence interval of 99% the ratio differs the most, this can also be seen for the PDFs in figure H.8. It is expected that more seeds are required for the results to converge. It can therefore be assumed, that in this case, only one of the two cases needs to be simulated to retrieve the statistics.

Table 6.7: Ratio between significant value and maximum moment (β) based on different confidence intervals

T_p [s]	β with 90% confidence interval	β with 95% confidence interval	β with 99% confidence interval

The stated hypothesis is validated, the statistics of the two selected cases are the same. To evaluate if this also applies to other input T_p for this configuration, 100 time-domain simulations of the other configuration are run for different wave peak periods. For each T_p between 3 and 12 seconds with increments of 1 second, the time-domain simulations are performed. In the next section, ratio β is shown for all the cases of the reference configuration.

Ratio β of the configuration

Below the different ratio β of the selected configuration, based on 100, three-hour time-domain simulations, can be found for the different T_p. In figure H.9, ratio β for the different T_p as well as the different confidence intervals are shown. Ratio β for 8 and 9 seconds are the same, as mentioned previously. The same applies for ratio β of 4 and 5 seconds. Ratio β for 3 and 7 seconds differ the most from the rest. This comes from the fact that these cases are close to the fundamental natural period of the crane and jack-up, respectively. The crane T_z is the highest in comparison to the ones of the jack-up and the sling. This results in a higher probability of an extreme, this increases the ratio between the significant value and the maximum moment. For a T_p of 7 seconds, the jack-up is dominant, this results in a lower ratio β as the probability of an extreme is lower. Ratio β for 6 seconds is almost identical to ratio β for 4 and 5 seconds. At last, ratio β for T_p of 10, 11 and 12 seconds are almost the same, and also close to ratio β of 8 and 9 seconds.

Looking at the shapes and statistics of the frequency domain spectra, in figure 6.11, the same trends can be found. For a T_p of 8 seconds and higher, the shapes are similar. For a T_p of 3 and 7 seconds, the crane or jack-up peak is dominant, resulting in the different ratio β.

When looking at the influence of the chosen confidence interval, the differences are quite significant. Particularly for a confidence interval of 99% the ratio is much higher, especially for a T_p of 3 seconds. It is chosen to base the calculation of ratio β on a confidence interval of 90%. As mentioned earlier, this is common practice in the offshore industry. Furthermore, the confidence interval of 90% is more accurate as the higher the confidence interval the more the tail of the distribution is inaccurate.

Fit of ratio β

Now that ratio β, for the reference configuration, has been calculated, it is investigated if it is possible to derive an equation to calculate ratio β based on the frequency domain spectrum. For this, the relation between the different nth-order moments, periods and ratio β, are looked at. From the relation between the different parameters, a fit is made of the ratio β of the reference configuration using the different parameters. Two parameters are chosen, these two parameters give the best representation of the behaviour of ratio β. The selected parameters are the zeroth-order moment and mean zero-crossing period of the frequency domain spectrum. Based on these two parameters, a fit of ratio β is made. In figure H.10a, the zeroth-order moment of the spectrum, for each T_p, is shown. Moreover, the mean zero-crossing period (T_z) of the spectrum for each T_p is shown, see figure H.10b.

Using the zeroth-order moment shown above and the mean zero-crossing period of the spectra, an equation is derived to calculate ratio β. The equation is as following:

$$\beta = \frac{0.45}{m_{0,\,\text{total}}} - 0.35 \cdot T_z + 3.9 \tag{6.9}$$

In figure H.11, ratio β calculated using 100 time-domain simulations and ratio β calculated using equation (6.9), are shown for each T_p of the reference configuration.

In figure H.11, it can be remarked that the two lines match quite closely. For now, it is decided that the small differences are acceptable. For cases with entirely different dynamics, the found equation is not validated. However, for now, the fitted equation is regarded as acceptable and is used to calculate ratio β for all the cases.

Significant value sensitivity

The significant value of the spectrum, which is used in the described method above, is the average significant value of the 100 seeds. Thus, there are 100 different seeds, which are all unique due to each sea-state having a different phase. The spread of the significant value needs to be checked, as the maximum moment to scale the statistic distribution is calculated using the significant value of one time-domain simulation. If the scatter is important, using one time-domain simulation can have a large influence on the calculated maximum moment using ratio β. In figure 6.12, the deviation from the mean of the significant value is shown for the different T_p. For all the cases, the deviation is quite similar, a maximum of around 10% from the mean, which is acceptable.

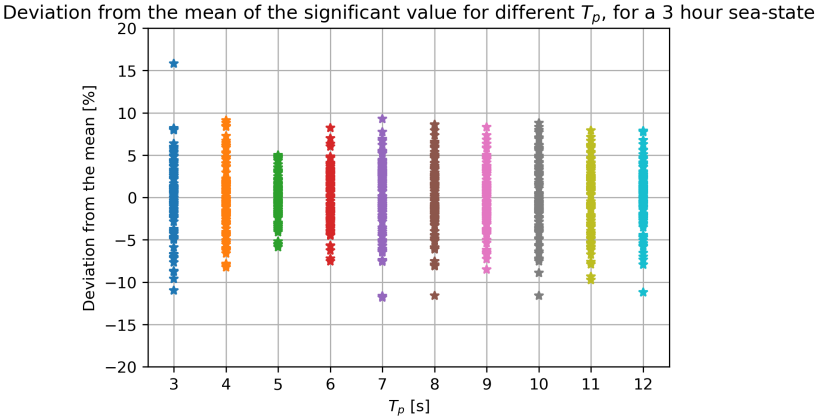

Figure 6.12: Distribution of the deviation from the mean of the significant value of the time-domain simulations

Conclusion

From the chosen reference configuration, two cases with similar frequency domain spectra are selected. The two found cases are investigated in frequency domain and time-domain. It is found that cases with similar frequency domain spectrum have the same statistics. Cases with the same statistics are found using the ratio of the different nth-order moments. Furthermore, it is checked that these cases have the same ratio between the maximum moment and the significant value (ratio β), which is the case. Thereafter, ratio β is calculated for all the different cases of the chosen configuration. A fit is made on the calculated ratio β. For now, it is assumed that the equation to calculate ratio β is also applicable for other configuration. Ratio β can be used to scale the normalized distribution of the maximum moment of each seed. For each case a distribution of the maximum moment is available. At last, the scatter of the significant value used to calculate ratio β is checked. The scatter is found to be acceptable.

6.2.6. Steps of the spectral analysis

Now that the method is checked for the reference configuration and that the equation to calculate ratio β based on the reference configuration is derived, the required steps can be summarized. The steps of the spectral analysis are as following:

1. Perform one time-domain simulation for each case
2. Calculate the frequency domain spectrum for each case

3. Group the cases with similar statistics
4. Run 100 time-domain simulations for one case of each group found in the previous step
5. Fit the distribution of the maximum moment of each seed
6. Normalize the fit of the distribution of the maximum moment of each seed
7. Calculate ratio β for each case using the derived equation
8. Scale the normalised distribution of the distribution found in the previous step using ratio β for each group

Performing the described steps, gives a distribution of the maximum moment of each seed, for each case, from this the APF can be calculated. In section 6.3, each step to go calculate the APF, from the different distributions of the maximum moment of each seed, are described.

6.3. Annual probability of failure

Now, for each case, the distribution of the maximum moment is known, the probability of the crane exceeding its maximum capacity can be calculated. For this, the maximum allowable moment in the heel point is calculated. This is based on the maximum allowable side-lead angle. In 5.3, the calculation of the maximum crane capacity (MCC) is explained.

From the different crane configurations, the probability of occurrence is known (exposure time and lifting occurrence). The probability of occurrence of each $H_s - T_p$ combination, that is used as input in SIMSEP, is also known. From this, the probability of failure of the crane at the heel point can be determined for each configuration. The probability of failure of the different configuration can then be combined to calculate the probability of failure on a yearly basis.

Below, each step for the calculation of the APF is described, considering all the different aspects that are shown in the flowchart in figure 6.13. First, the probability of the JU and crane configuration are considered. Then the probability of the sea-state and of exceeding the MCC are added. This gives the probability of failure of one wind turbine installation. This probability is multiplied by the total number of yearly lifts. The different steps will be elaborated in the following sections.

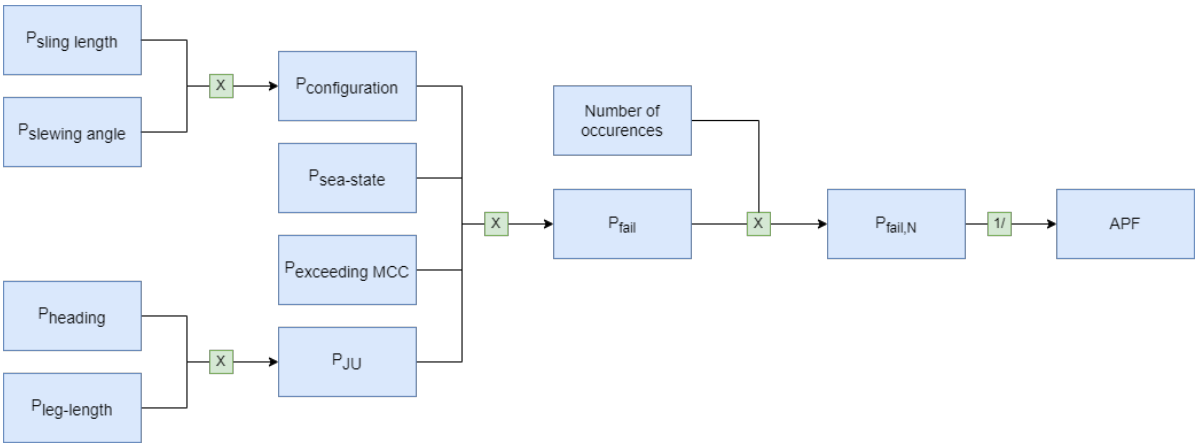

Figure 6.13: Overview of the different probabilities considered to calculate the APF

6.3.1. Probability of failure of one case

To calculate the probability of failure, the distribution of the maximum moment of each seed is taken. The fit made previously is taken to get the PDF. Using the PDF, the area is calculated of the probability that the moment is below the MCC value calculated in section 5.3. From this, the probability that the moment exceeds the MCC value can be calculated.

$$P_{exceeding\,MCC}(M_{max} > MCC) = 1 - P(M_{max} < MCC) \tag{6.10}$$

Where:

$P_{exceeding\,MCC}$ = Probability of failure
M_{max} = Maximum moment
MCC = Maximum crane capacity

This gives the probability of failure for one occurrence of the case. This is performed for the distribution of maximum moment of each seed, for each case.

6.3.2. Probability of failure of multiple occurrences

Now that the APF for one yearly occurrence of the case is calculated, the APF of N number of occurrences can be calculated. For this, each individual probability of failure is summed before calculating the failure return period. This is because each operation can be seen as an independent event, so the probability of failure of each single lift is not affected by the previous or the following lift. In the equation below, the calculation for the failure probability of one case with N occurrences is shown.

$$P_{fail,N} = P_{exceeding\,MCC} \cdot N \tag{6.11}$$

Where:

$P_{fail,N}$ = Probability of failure of N occurrences
N = Number of occurrences

The dependence of the APF on the number of yearly occurrences can be seen in figure 6.14, the APF has a steep drop for an increasing number of yearly occurrences.

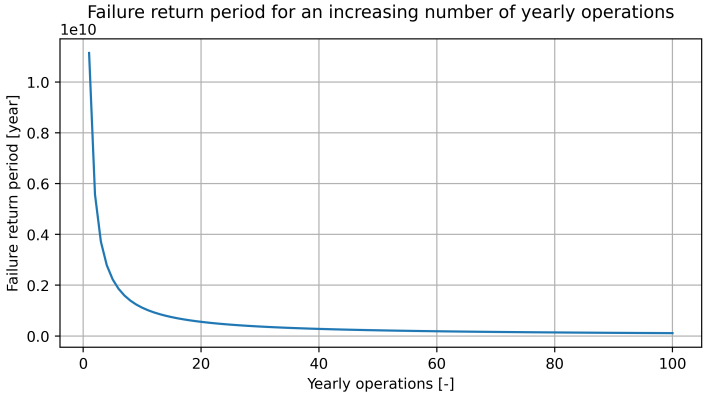

Figure 6.14: Failure return period for an increasing number of yearly operations

6.3.3. Probability of the sea-state

To consider the probability of the different sea-states used as input for the SIMSEP time-domain simulation of the jack-up motions, the distribution shown in section 4.1 is used. So, the probability of failure of the case is multiplied by the probability of occurrence of the used $H_s - T_p$ combinations.

$$P_{fail,1} = P_{fail,N} * P_{H_s - T_p} \tag{6.12}$$

Where:

$P_{fail,1}$ = Probability of failure considering the $H_s - T_p$ combination
$P_{H_s - T_p}$ = Probability of occurrence of the $H_s - T_p$ combination

6.3.4. Probability of multiple crane and jack-up configurations

Now that the APF for one crane configuration is calculated, the influence of multiple crane configurations needs to be looked at. For each lift type, there are multiple sling lengths and slew angles, this needs to be accounted for. These are dependent events, so only one sling length and one slew angle can occur at the same time. Therefore, the probability of failure needs to be multiplied by the probability of occurrence of the sling length and slew angle.

For the jack-up, the same is applicable, for each configuration the jack-up can have a different incoming wave direction relative to the jack-up or a different leg length. These needs to be considered as dependent events. The probability of these different set-ups is known, so this can also be included in the calculation of the APF. Below, the different equations to calculate the probability of failure, accounting for the probability of the crane and jack-up configurations.

$$P_{fail,2} = P_{fail,1} * P_{crane\ configuration} * P_{JU} \tag{6.13}$$

$$P_{crane\ configuration} = P_{sling\ length} * P_{slewing\ angle} \tag{6.14}$$

$$P_{JU} = P_{leg\ length} * P_{wave\ direction} \tag{6.15}$$

Where:

$P_{fail,lift}$	=	Probability of failure considering all required probabilities
$P_{sling\ length}$	=	Probability of sling length
$P_{slewing\ angle}$	=	Probability of slewing angle
$P_{wave\ direction}$	=	Probability of occurrence of the wave direction relative to the jack-up
$P_{leg\ length}$	=	Probability of occurrence of leg length

At last, the probability of failure of the different lift types needs to be combined. The same principle applies as taking into account multiple yearly operations when looking at the lifts of different components. This is because, each lift of a different component can also be seen as an independent event. Therefore, each probability of failure can be summed.

$$P_{fail,all} = \sum P_{fail,lift} \tag{6.16}$$

6.3.5. Failure probability to annual probability of failure

To calculate the APF, the inverse is taken of the previously calculated probability of failure, see the equation below.

$$APF = \frac{1}{P_{fail,all}} \tag{6.17}$$

7

Results

Now that the input, models and the methodology are explained, the resulting results can be discussed. Using the methodology described in chapter 6, the following results are obtained, as well as the sensitivity analyses:

1. Maximum moment from time-domain simulations
2. Results of the spectral analysis
3. Assumptions and simplification of the probabilistic model
4. Annual probability of failure results
5. Sensitivity analysis of the exposure time on the APF
6. Sensitivity analysis of the maximum crane capacity on the APF

First, the maximum moment based on the time-domain simulations is shown. Next, the results of the spectral analysis to find cases with similar statistical descriptions are shown. The assumptions and simplifications used for the probabilistic model are discussed. From this, the APF is calculated and at last two sensitivity analysis are performed. First, the sensitivity of the APF for different exposure times and then for different MCC.

7.1. Maximum moment from time-domain simulations

The maximum moment is calculated for one configuration for each H_s of 3 meters and T_p of 3 to 12 seconds, with steps of 1 second. For these cases, 100 time-domain simulations are performed, to calculate the absolute maximum moment in the heel point. The configuration is a nacelle lift with a slewing angle of 90 degree and the waves with an incidence angle of 0 degree towards the jack-up. The slewing angle of the crane is perpendicular to the wave heading to get maximum excitation. The sling length is 170 meters, which is when the nacelle is just above the deck. This is the same as the reference configuration used in the methodology. Below, the best fit of the distributions of these cases are shown and an overview is given of the maximum moment distribution with some key parameters. At last, a conclusion is given.

7.1.1. Best fit of maximum moment distribution

In the methodology, a fit is made of the distribution of the maximum moment of each seed. The absolute maximum moment, of each seed, is taken, as it can be either in negative or positive direction. To find which fit describes the best the distribution of maximum moment of each seed, multiple different probability distribution types are investigated and the R^2 is calculated. These are:

- Normal distribution
- Rayleigh distribution
- Gumbel distribution
- Exponentiated Weibull distribution
- Log-normal distribution

In figure H.16, the different types of probability distribution are shown of the PDF of the maximum moments of each seed. The fit to find the best probability distribution has been made using the CDF of the maximum moment. It can be remarked that the log-normal and Rayleigh distribution are the least representative. The other three types of probability distribution match the distribution of maximum moment of each seed better. For this, the R^2 value of each probability distribution type is calculated. This value gives the coefficient of determination, which is a measure of the goodness of the fit.

In table 7.1, the R^2 value for different types of probability distributions are shown. this is done for multiple T_p, it can be seen that the maximum moment distribution, in most of the cases, is best described by an Exponentiated Weibull distribution. For the cases where a Gumbel distribution is a better fit, the difference in R^2 is negligible compared to the Exponentiated Weibull distribution. For simplicity, it is chosen to only use an Exponentiated Weibull distributions to describe the statistical properties of the distribution of maximum moment of each seed.

Table 7.1: R^2 value of the different probability distribution types, for different T_p

Distribution type	Normal	Rayleigh	Gumbel	Exponentiated Weibull	Log-normal
T_p [s]	R^2	R^2	R^2	R^2	R^2
3	0.506	0.591	0.655	**0.662**	0.660
4	0.716	0.790	0.812	**0.822**	0.762
5	0.825	0.852	0.854	**0.865**	0.842
6	0.705	0.806	0.814	**0.840**	0.754
7	0.743	0.757	0.759	**0.782**	0.752
8	0.776	0.837	**0.854**	0.842	0.809
9	0.776	0.834	0.853	**0.844**	0.812
10	0.855	0.902	**0.912**	0.910	0.889
11	0.734	0.872	0.843	***0.887***	0.791
12	0.816	0.928	0.922	**0.931**	0.861

In appendix C, the figures of the distribution of maximum moment of each seed and the fitted probability distributions are shown for T_p of 3 to 12 seconds. From these distributions, it can be remarked that for a T_p of 3 seconds, the spread in maximum moment is the largest. This is due to the low T_p of the sea-state, resulting in many waves that are close to the fundamental natural period of the crane. The other maximum moment distributions and probability distributions are more narrow banded.

7.1.2. Maximum moment overview

In figure H.17, the 90% confidence interval maximum moment and significant value is plotted for different T_p. The results are based on a three-hour exposure time. It can be remarked that for a T_p of 3 seconds the maximum moment is the highest. This is because the fundamental natural period of the crane is closest to the excitation period. For high T_p, the moment is decreasing, the reason for this is discussed in section 7.1.3.

In table 7.2, the significant value, variance and 90% confidence interval maximum moment are listed for multiple T_p. The significant value and the variance are the mean of the 100 time-domain simulations. The 90% confidence interval is retrieved from the fitted Exponentiated Weibull distribution. It can be seen that the higher the significant value, the higher the 90% confidence interval value and variance. This trend can also be seen in the figure above. This relation between the significant value and 90% confidence interval maximum moment, is used for ratio β.

Table 7.2: Significant value, variance and 90% confidence interval of the maximum moment distributions for different T_p

In figure H.17, it can be remarked that the highest maximum moments occur at a T_p of 3 and 7 seconds. For a T_p of 3 seconds, the excitation period is close to the natural period of the crane, resulting in the most dynamic response of the crane. For a T_p of 7 seconds the excitation period is the closest to the jack-up natural period, resulting in the most dynamic response of the jack-up. For increasing T_p, the maximum moment decreases, even so the fundamental natural period of the sling is getting closer to the excitation period. The loads due to the dynamic response of the crane are negligible for higher T_p in these cases.

In section 7.2, figure H.18, the spectra of this configuration for the different $H_s - T_p$ combinations can be found. From these spectra, the relation between the frequency domain spectra and the maximum moment can be explained.

7.1.3. Relation between spectra and maximum moment

From the maximum moment shown in figure H.17, two cases stand-out, for a T_p of 3 and 7 seconds. In figure H.18a and H.18b, the frequency domain spectra of the two mentioned cases are shown. For a T_p of 3 seconds, it is found that the maximum moment is the highest. From the frequency domain spectrum, it can be remarked that the crane component is dominant. The crane component has the lowest mean zero-crossing period, compared to the jack-up and sling. Therefore, there are the most peaks in the time-domain, resulting in a high probability of an extreme. Furthermore, the T_p of 3 seconds with an H_s of 3 meters results in very steep waves, causing a lot of dynamic response of the crane. For a T_p of 7 seconds, the jack-up component is the highest, this is due to the wave excitation period being the closest to the jack-up fundamental natural period.

7.1.4. Conclusion

The best statistical fit of the distribution of maximum moment of each seed is investigated. It is concluded that for an Exponentiated Weibull distribution, the maximum moment distribution is best described. It is established that for a T_p of 3 seconds the maximum moment is the highest. In this case, the crane response is dominant. For the other T_p, the maximum moment is at least half the size. A relation can be seen between the significant value and the maximum moment. The higher the maximum moment, the higher the significant value and variance of the time-domain simulation.

7.2. Results of the spectral analysis

Confidential

7.3. Assumptions and simplification of the probabilistic model

To calculate the APF, some assumptions and simplification are made for the probabilistic model:

1. Because no extra time-domain simulations are performed, only the statistical distributions of the configuration used in the methodology are used. The spectral analysis is performed to match cases with similar statistics, but to match the statistical distribution of the maximum moment of the cases that have been run, to the other cases, another method is used. The cases with the same T_p are assumed to have the same statistical distributions. Above it is found that this does not apply for all cases, but for now, this is accepted.
2. For the water depth, it is found that the statistics are different for each water depth. Therefore, in the probabilistic model, only a water depth of 60 meters is considered.
3. In the methodology, the equation for ratio β is based on only one configuration. It is, for now, assumed that this equation is also valid for configurations with different statistics.

7.4. Annual probability of failure Results

Now that for all the different configurations, the frequency domain spectra have been looked at and cases with the same statistics have been identified, the APF can be calculated. The following steps of the APF calculation will be shown:

1. Overview of probabilities
2. Annual probability of failure with only probability of exceeding maximum crane capacity
3. Annual probability of failure with probability of the sea-state
4. Annual probability of failure of the different configurations
5. Annual probability of failure for all the configurations

7.4.1. Overview of probabilities

In table 7.3, an overview is given of the different configurations and the different parameters for the calculation of the APF. The exposure time, the number of occurrences per year, the number of different sling lengths and the number of different slewing angles are given. In each configuration, the slewing angle of the crane is perpendicular to the wave heading. The number of slewing angles considers the different wave headings. At last, in the spectral analysis different water depth are looked at, for the calculation of the APF only a water depth of 60 meters is considered.

Table 7.3: Overview of the different key parameters that make up the probability of the different configurations

Lift type	Exposure time [min]	Number of lifts [-]	Number of sling lengths [-]	Number of slewing angles [-]	Number of occurrences in a year [-]
Tower	-	1	1	3	82
Nacelle	-	1	2	3	82
Blade	-	3	2	3	246
Yoke	-	3	2	3	246
Luffing	-	1	1	3	164
Waiting	-	1	2	3	246

In section 4.3.1, the number of installed wind turbines on a yearly basis is defined to be 82. Each wind turbine has three blades, this results in 246 blade lifts. Before each blade lift, the crane is waiting with the blade yoke in the hook, so there are 246 yoke lifts. The crane is luffing twice for each wind turbine installation. Once at the beginning and once at the end of the lifting operation, with an exposure time of three-hour. For the waiting time, a three-hour exposure time is assumed in between each lift. This results in three different occurrences for each wind turbine installation.

7.4.2. Annual probability of failure of exceeding maximum crane capacity

The probability of failure of each case is calculated based on the scaled normalized distribution of the maximum moment. Ratio β is used to calculate the 90% confidence interval maximum moment, which is used to scale the distribution. The time-domain simulations for the spectral analysis are run for a H_s of 3 meters. The amplitude of the maximum moment is linearly dependent on the H_s. Because the wave heights remain small and therefore only inertia terms are considered in the wave load calculations, section 2.2.1. For a H_s of 1 meter, the maximum moment is divided by three and for a H_s of 2 meters, the maximum moment is divided by 1.5. In table 7.4, the probability of exceeding the MCC without accounting for the sea-state probability and number of occurrences are shown. It can be remarked that the difference in APF is significant between each lift type. The tower lift has the lowest APF and the waiting configuration the largest, with a factor 123. The blade and yoke lift have the same statistics but other exposure times, the difference in APF is significant, a factor 19. The influence of the exposure time on the APF is expected to be large based on these results. In section 7.5, a sensitivity analysis is performed on the exposure time. It can be remarked that the APF for the waiting and luffing configuration are the largest, this is due to the long exposure time of these configurations. As said about the difference between the yoke and the blade lift, the exposure time is an important parameter for the APF.

Table 7.4: APF for each lifting operation without accounting for the sea-state probability and number of occurrences

Lifting operation	APF [years]
Tower	1,969,869
Nacelle	806,523
Blade	336,088
Yoke	18,207
Luffing	16,373
Waiting	15,454

In appendix F, the different APF of each configuration for each $H_s - T_p$ combination are shown. The APF is without accounting for the probability of the sea-state and the number of occurrences. From the table, it can be remarked that the APF for a T_p of 3 seconds is the largest for most of the configurations. When there is no value in a cell, the tail of the distribution is too small to calculate the probability of exceeding the MCC. In these cases, it is assumed that the probability of failure is zero.

7.4.3. Annual probability of failure with probability of the sea-state

Now that the probability of exceeding the MCC is calculated, the probability of occurrence of the sea-state needs to be accounted for. The four locations, selected in section 4.1, are used to define the probability of occurrence of each different $H_s - T_p$ combination. In appendix E, the probabilities of each $H_s - T_p$ combination are shown. The probability of exceeding is calculated for each $H_s - T_p$ combination and then multiplied by its probability of occurrence. In table 7.5, the APF for each lifting operation are shown, accounting for the sea-state probability. It can be seen that the APF increases considerably, this is because in most cases where the probability of exceeding the MCC is higher, the probability of the sea-state is very small.

Table 7.5: APF of each lift type, accounting for the sea-state probability

Lifting operation	APF [years]
Tower	51,229,122,261
Nacelle	20,798,512,811
Blade	870,3678,236
Yoke	406,705,660
Luffing	368,489,597
Waiting	344,538,200

In appendix F, the different APF of each configuration for each $H_s - T_p$ combination are shown. The APF is with the probability of occurrence of the sea-state and without the number of occurrences of the

lifts.

7.4.4. Annual probability of failure of the different configurations

At last, the number of yearly occurrences of the lift needs to be accounted for. The number of occurrences of each lift type can be seen in table 7.3. In table 7.6, the APF for each lift type, accounting for the number of occurrences, are shown. It can be remarked that the APF gets lower. Especially, for cases with a larger number of occurrences, like the yoke and blade lift.

Table 7.6: APF of the different lifting operations

Lifting operation	APF [years]
Tower	624,745,393
Nacelle	253,640,400
Blade	35,380,806
Yoke	1,653,275
Luffing	2,246,888
Waiting	1,400,562

7.4.5. Annual probability of failure for all the configurations

Now that the different probabilities are known, the APF of the crane in normal operations can be calculated. This answers the research question of the APF of the crane in normal operation.

The APF is 556,258 years.

This is much higher than the minimum APF of 10,000 years required from class. This APF is based on the statistics of only one configuration for different $H_s - T_p$ combinations. It is assumed, for the moment, that the other cases have the same statistical description. However, as can be seen in section 7.2, there are multiple different groups of cases with the same statistics. Therefore, the assumption of only using the statistical distributions of one configuration is inaccurate.

The APF is defined by lifting operations with long exposure time and high number of occurrences, like the yoke lift and when the crane is waiting. Lifting operations with short exposure time, like a tower, blade and nacelle lift, have a high APF. The influence of the exposure time on the APF is large. In section 7.5, the influence of the exposure time is investigated. Next, the influence of the MCC on the APF is investigated. Because, the MCC is based on an assumption, it is relevant to investigate what the influence of the MCC is on the APF.

7.5. Sensitivity analysis of the exposure time on the APF

To check how different parameters affect the APF, an investigation is made on the exposure time. To calculate the final APF, in section 7.4, the found exposure times in section 4.3.2, are used for each configuration. To quantify the influence of the chosen exposure times on the APF, three different exposure times are looked at, one, two and three-hour. The influence of the exposure time on the maximum moment, maximum moment distribution and finally on the APF of the crane are reviewed. The items are listed below:

1. Influence on maximum moment
2. Influence on the distribution
3. Influence on APF
4. Conclusion

7.5.1. Influence of the exposure time on the maximum moment

The influence of the exposure time on the maximum moment is investigated. When changing the exposure time of the configuration, the distribution of maximum moment of each seed, converges for another seed size. Because no more time-domain simulation are performed for this sensitivity analysis,

the maximum available seed size will be used. 100 seeds with a three-hour exposure time are available, for the smaller exposure times, these time-domain simulations have been separated into one and two-hour pieces. This means that for a three-hour exposure time, 100 seeds are used, for a two-hour exposure time, 150 seeds are used and for a one-hour exposure time, 300 seeds are used. In figure H.14, the 90% confidence interval maximum moment of the distribution of maximum moment of each seed, for the different T_p and the selected exposure times are shown. The same configuration is used as the one used to in the methodology, see section 6.2.5.

It can be seen that the influence of the exposure time on the maximum moment is the highest for a T_p of 3 seconds. For the other T_p, the differences are small. As expected, the maximum moment gets smaller for a shorter exposure time. There are fewer peaks in a shorter exposure time, resulting in a lower probability of a maximum. It can be seen in section 7.5.2, the distribution changes for different exposure times, the tail gets smaller for shorter exposure times.

7.5.2. Influence of the exposure time on the distribution

The difference in 90% confidence interval maximum moment for different exposure times, shown in figure H.14, is caused by a change in maximum moment distribution. In figure H.15, the difference in maximum moment distribution is shown for a T_p of 3 seconds. These distributions are an Exponentiated Weibull fit of the maximum moment. The three distributions are different, the peak moves to the left and for an exposure time of one-hour becomes smaller for a shorter exposure time. This is because in a shorter time-frame, the probability of an extreme is lower, resulting in the distribution moving to the left.

In appendix G, the distribution for the others T_p are shown. For all T_p, the distribution moves to the left for decreasing exposure times.

7.5.3. Influence on the exposure time on the APF

In table 7.7, the APF are shown for different exposure times of the lifts. It can be seen that the exposure time has a big influence on the APF. If the exposure time is one-hour, the APF is 22 times higher than for an exposure time of three-hour.

Table 7.7: Influence of exposure time on APF

Exposure time [hour]	1	2	3
APF [years]	9,007,908	950,430	395,696

7.5.4. Conclusion

For decreasing exposure times, the APF also decreases. This is expected as in a shorter time-frame less peaks can occur, resulting in a lower probability of an extreme. The difference in APF is significant between the different exposure times. In section 4.3.2, the different exposure times of the different lifts were defined. These exposure times are based on a few measured lifts. Due to the limited available data, the exposure times are not very accurate. It is found that the exposure time has an important influence on the exposure time. Because the MCC is far away from the maximum moments calculated in the heel point, the probability of exceeding the MCC is calculated far in the tail of the distribution. This results in large differences in the APF between the different exposure times. This also explains the small difference in the 90% confidence interval maximum moment, which is less far in the tail of the distribution.

7.6. Sensitivity analysis of the maximum crane capacity on the APF

The found APF is high compared to the allowable APF of 10,000 years, therefore, the MCC sensitivity on the APF is checked. For the found APF, the MCC is calculated for a side-lead angle of 0.5 degree. Two other side-lead angles are investigated, 0.1 and 0.2 degrees. For these two side-lead angles, the MCC is calculated and then the new APF's are calculated. These will be compared to the APF with an allowable side-lead angle of 0.5 degree. In table H.1, the MCC for different side-lead angles are shown.

From the different MCC, the APF can be calculated. In table 7.8, the APF are shown for the three different side-lead angles. The difference in APF is significant. For the two smaller side-lead angles

the APF is below the minimum APF of 10,000 years. For a side-lead angle of 0.1 degree, the crane will fail within a year.

Table 7.8: APF for smaller allowable side-lead angles

Side-lead angle [degree]	0.1	0.2	0.5
APF [years]	0.12	136.48	556,258

In table 7.9, the APF of each lifting operation are shown. As remarked before, operations with a long exposure time and high number of occurrences have the largest APF. For a side-lead angle of 0.2 degree, the tower and nacelle lift have a higher APF, but still half the minimum required APF. For the other operations, the APF remains very low.

Table 7.9: APF for each lifting operation for different MCC

	APF [years]		
Lifting operation	0.1 degree side-lead	0.2 degree side-lead	0.5 degree side-lead
Tower	6.94	4,418.37	624,745,393
Nacelle	2.92	5,511.87	253,640,400
Blade	0.67	566.16	35,380,806
Yoke	0.61	491.65	1,653,275
Luffing	0.54	1,048.21	2,246,888
Waiting	0.36	461.92	1,400,562

7.6.1. Conclusion

It can be concluded that the chosen MCC has a big impact on the APF. For a side-lead angle of 0.1 and 0.2 degree, the APF is largest. In these two cases, the APF is larger than what is seen as acceptable. For a side-lead angle of 0.1 degree, the crane will fail within less than a year. It is advised to further investigate what an acceptable side lead angle is, as the results are very dependent on this allowable side-lead angle.

8

Conclusion

In this chapter, the overall conclusion will be given. the research questions stated in chapter 1 will be answered. A discussion about the results and recommendations for future work will be given as well.

8.1. Conclusion

Below, each research question is answered:

Which external loads need to be accounted for the dynamic response of the crane?
In this research, the effect of the load due to the crane dynamic response is researched. The dynamic response of the crane is caused by the motions of the jack-up. The motions of the jack-up are caused by the wave induced excitations on the legs of the jack-up. The wave input is based on the long-term wave statistics of relevant locations.

Currently, this load is not yet considered for the design of the crane. Therefore, the maximum capacity of the crane for to the dynamic response of the crane needs to be defined. For this, the current method to define the maximum static capacity of the crane is taken and redefined for dynamic loads. This is based on the maximum side-lead angle of the crane, which is taken to be 0.5 degree. The location is at the heel point of the crane. This side-lead angle implicitly considers the wind load and deadweight of the crane. This side-lead angle is used in the static model to define the failure probability of the crane.

Which jack-up and crane configurations need to be accounted for, to mimic the operational profile of a jack-up installing wind turbines?
An extensive study is performed on measurement data of a smaller jack-up, the different lift types are identified. The different slewing and luffing angles of each lift type are retrieved. Next to that, the exposure time of each lift is investigated and the statistical distributions are looked at. Six different crane configurations are selected, a tower, nacelle, yoke, blade, waiting and luffing configuration.

Are the present assumptions in the NX-motion crane model correct?
Three different assumptions in the crane model in NX-motion are investigated:

1. It is investigated if the current assumption to model the boom hoist wire rope as a simple spring, without considering its mass, is correct. For this, the boom hoist wire rope is modelled as a multiple mass-spring elements and the catenary effects of the wire rope are investigated. A static analysis is done for multiple luffing angles, for each luffing angle no catenary effects are found. Due to the low number of oscillations in the dynamic response, it can also be concluded that the boom hoist mass has a negligible effect on the crane dynamic response. It is concluded that the current assumption, of modelling the wire rope as a spring, is correct.

2. Current practice is to model the sling configuration as a simple pendulum with a point mass at its end. It is investigated how the sling dynamic response changes when adding more detail to the sling configuration. Multiple configurations are investigated and their fundamental natural period are compared. It is found that the current set-up is the most conservative. To consider the difference caused by adding more detail, it is chosen to scale the sling length of the simple

pendulum configuration. During the investigation of the dynamic response of the crane due to the jack-up motion, it is found that the dynamic response of the sling has a negligible influence on the crane dynamic response. Therefore, the modelling of the sling configurations has little influence on the dynamic response of the crane.

3. Non-linear sling couplings are investigated. It is expected that these occur when there are off-diagonal inertia terms in the inertia matrix of the load in hook. It is found that the coupling is negligible and it is not required to consider the coupling for the dynamic response of the sling.

Based on a spectral analysis of the different jack-up and crane configurations, is it possible to limit the required number of time-domain simulations?
From the frequency domain spectra of the different configurations for different $H_s - T_p$ combinations, cases with similar statistical descriptions are researched. For this, the ratio of the zeroth-order moment between the different components (crane, jack-up and sling) are investigated. It is found that for cases with similar ratios, the statistics are the same. Using this, cases with the same statistics are grouped. For each group of cases, one of the cases is simulated in the time-domain for several seeds. Several seeds are required, due to the random nature of the input sea-states. For convergence of the results, it is found that 100 seeds are required. From this, the distribution of the maximum moment can be derived. This gives the statistical description of each group of cases.

It is expected that this method applies to the different crane and jack-up configurations. The different dynamic components (jack-up, crane and sling) remain approximately the same. Only the amount of energy and the dominant component changes for the different configurations.

Is it possible to calculate the expected maximum moment based on a spectral analysis?
For the cases where one time-domain simulations is performed, the distribution of the maximum moment needs to be scaled. For this, the distribution of the maximum moment of each seed, of the cases of the group for which the required seeds are run, is normalised. To scale these distributions, the ratio between the significant value and the maximum moment is researched. It is found that high maximum moments occur for cases with large significant values and that the ratio is not much larger for these instances.

For one configuration, these ratios are calculated, using time-domain simulations. An equation is derived to calculate this ratio based on the frequency domain spectrum. Using this equation, the normalized distribution of the maximum moment can be scaled for the cases where only the frequency domain analysis is performed. This method is valid when it is possible to find cases with the same statistics using a spectral analysis. As mentioned above, it is found that for the investigated configurations, groups of cases with the same statistics are found.

What is the annual probability of failure (APF) of the crane, considering the relevant loads, crane operations and the crane resistance?
The APF of the crane during normal lifting operations is 556,258 years, based on the assumptions made for the base case of this thesis. The found APF is much smaller than the maximum APF of 10,000 years. In normal operation, the probability of failure of the crane is negligible. No crane configurations has a maximum moment that comes close to the maximum crane capacity (MCC). When the wave peak periods (T_p) comes close to the fundamental natural period of the crane, the maximum moment in the heel point is the largest. However, the probability of the sea-state is very small for these T_p. The influence of the sling on the dynamic response of the crane is looked at. It is found that the contribution of the dynamic response of the load in hook is only a small contribution to the total load. The dynamic response of the crane is dominant for the total load. It could therefore be argued that modelling a more detailed sling configuration will have negligible influence on the APF. The load in hook will dampen the motion of the crane tip due to the low dynamic response of the sling.

How is the APF influenced by different assumptions and input?
A sensitivity analysis is performed on the APF of the crane, different exposure times and MCC are checked.

1. It is found that depending on the exposure time chosen for each lift, the APF changes significantly. Between a one and three-hour exposure time, there is a factor 22 difference.

2. The MCC is based on a maximum dynamic side-lead angle of 0.5 degree, for smaller side-lead angles the APF is also checked. For 0.1 and 0.2 degree side-lead angle, it is found that the APF

is below the allowable minimum APF of 10,000 years. The sensitivity of the APF to the different side-lead angles is considerable.

From the sensitivity analysis, it is concluded that depending on the chosen exposure time of the lift and the chosen MCC the result vary significantly. The MCC is located far in the tail of the distributions of the maximum moment of each seed, resulting in significant differences in the results. Therefore, the outcome of the probabilistic model is very sensitive to the different inputs.

8.2. Discussion and recommendations

A method is developed to select cases with similar statistics, based on the frequency domain spectrum of the different configurations. For this, the amount and location of energy in the frequency domain spectra is investigated. Currently, this method is checked for only one crane configuration, a nacelle lift with a long sling length. More research is required to find out if this method is also applicable for configurations with different dynamic responses.

It is found that most of the loads in the crane are caused by the vibration of the crane. For the MCC definition, the dynamic side-lead angle is taken. Currently, the crane is designed based on a static side-lead angle. From the conclusion that the loads are due to the crane vibration, this dynamic side-lead angle needs to come on top of the static side lead angle, already used in crane design.

The MCC is based on a maximum side-lead angle of 0.5 degree, this angle is based on an assumption. The loads of the wind and the deadweight of the crane are implicitly considered in the chosen side-lead angle. From the sensitivity analysis, it is found that depending on this side-lead angle, the APF varies a lot. Currently, within the offshore industry, the dynamic response of the crane is not yet considered for the MCC. From classification societies, only the MCC due to the statics side-lead angle is defined. It is advised to develop a more profound understanding of the allowable dynamic side-lead angle or to define a better crane capacity for loads due to dynamic response of the crane. Further research is required to check if this assumption is valid.

From the findings of this thesis, some recommendations for future work are given. The results from the sensitivity analysis indicated that the APF varies a lot depending on the exposure time. It is recommended for future studies to minimize this sensitivity. The following items are expected to increase the accuracy of the probabilistic model.

1. From the sensitivity study on the influence of the exposure time on the APF, it is concluded that the exposure time has a significant influence on the APF. Currently, the measurement data of a smaller jack-up is used and only a limited number of lifts are available. To increase the accuracy of the exposure time of the different lift types, a larger set of measurement data should be investigated. This would increase the accuracy of the fit of the exposure time, resulting in a more accurate confidence interval of the statistical description of the exposure times, used for the APF calculations. This is especially the case for the lifts of the blades and yoke. The influence of the dynamic response of the crane and wind load on these components is high, resulting in significant variations in exposure time and a poor statistical fit. Next to using more measurement data, it is recommended to use measurement data of a NG-20000X jack-up. These jack-ups are currently being built and have an extensive measurement system on-board. It is expected that in the future, more data will be available to create a more accurate operational profile.

2. Next, all the cases have been put into the same group and it is assumed that cases with the same T_p have the same statistical description. This assumption is not accurate, from the frequency domain spectrum it can be seen that in some cases different statistics occur. Using the method developed to find cases with similar statistics, groups of cases with similar statistics need to be made. Expanding this method will increase the accuracy of the APF.

3. To increase the accuracy of the equation used to calculate ratio β, the formula should be validated for configurations with different statistical descriptions and, if required, be improved.

4. For the slewing angle and wave heading, only three wave headings are considered and for each case the slewing angle is perpendicular to the wave heading. For a more accurate result, more slewing angles should be included in the probabilistic model.

5. In the present probabilistic model, only two sling lengths are considered. Only the maximum and minimum sling length of each configuration are used. To increase the accuracy of the APF, more sling length should be considered.

6. The probability of the wave direction is taken to be the same for all three directions. The same is done for the different slewing angles and sling lengths. Further investigation is required to better define these probabilities and should be incorporated in the probabilistic model, as this has an influence on the APF.

7. Only one water depth is considered for the calculation of the APF, it is recommended to also consider other water depths. The water depth has an influence on the fundamental natural period of the jack-up and this influences the crane response. Furthermore, the probability of each water depth should be investigated and considered in the probabilistic model.

At last, some possible future expansions of the crane model in NX-motion are given:

1. For the lifting of wind turbine blades, tugger lines are used to limit the motions and to guide the blade into the hub. In the current crane model, these tugger lines are not yet incorporated. These could be added to the model to add stiffness to the configurations when blades are lifted. Due to the small dynamic response of the sling, the fundamental natural period of the crane will change when adding tugger lines.

2. Currently, the wind load on the load in hook and on the crane is implicitly considered in the chosen side-lead angle. The low wind speed allowed during lifting operations has a low dynamic component. However, incorporating the wind load in the dynamic excitation of the crane will increase the accuracy of the model.

Bibliography

[1] International Standards Organizations (ISO). *Petroleum and natural gas industries - Site specific assessment of mobile offshore units*. ISO 19905-1. second edition 2016.

[2] D. Ahn et al. “Comparative evaluation of different offshore wind turbine installation vessels for Korean west–south wind farm”. In: *International Journal of Naval Architecture and Ocean Engineering* 9.1 (2017), pp. 45–54. ISSN: 2092-6782. DOI: https://doi.org/10.1016/j.ijnaoe.2016.07.004. URL: https://www.sciencedirect.com/science/article/pii/S209267821630437X.

[3] T. Blankenstein. *Dynamics of Structures Mitigative Measures for Jackups Subjected to Earthquakes*. TU Delft, 2020.

[4] B. van Daalen. “A study of a tub crane with an unconventional quadruple hook arrangement”. Technical University Delft, July 2016. URL: https://repository.tudelft.nl/islandora/object/uuid%3Af095b21f-1c9e-40f1-b8e0-813342ae44c5?collection=education.

[5] A. van Dalfsen. “Integral soil-jack-up modelling - Modelling site-specific jack-up response and performing safety assessment”. TU Delft, May 2016. URL: https://repository.tudelft.nl/islandora/object/uuid%3A7e853a7f-834c-46ee-8bc4-76fd991bf9af?collection=education.

[6] N. van Engelen. “Earthquakes and offshore wind turbine installation”. TU Delft, June 2021. URL: https://repository.tudelft.nl/islandora/object/uuid%3A364bccc8-e109-4129-9229-c55c5ad3dec5?collection=education.

[7] GustoMSC and G.J. Gründlehner. *Jack-Up time domain analysis program SIMSEP*. Tech. rep. Apr. 1995.

[8] T. Haniszewski. “Modeling the dynamics of cargo lifting process by overhead crane for dynamic overload factor estimation”. In: *Journal of Vibroengineering* 19 (1 Feb. 2017), pp. 75–86. ISSN: 1392-8716. DOI: 10.21595/JVE.2016.17310. URL: https://www.extrica.com/article/17310.

[9] J. S. Hoving. *Bottom founded offshore structures, Environmental loading*. Mar. 2021. URL: brightspace.tudelft.nl.

[10] IEA. *Offshore Wind Outlook 2019*. Tech. rep. Nov. 2019. URL: https://www.iea.org/reports/offshore-wind-outlook-2019.

[11] J.M.J. Journée and W.W. Massie. *Offshore Hydromechanics*. Second Edition. 2008.

[12] M. Koole. “Dynamic Analysis on Failure Modes of Tub Mounted Cranes”. Technical University Delft, Aug. 2015. URL: https://repository.tudelft.nl/islandora/object/uuid%3A4d585c0f-8382-4860-898c-272ceea741eb?collection=education.

[13] J. Linthorst. “Seismic Analysis of Cranes on Jack-Ups”. TU Delft, July 2019. URL: https://repository.tudelft.nl/islandora/object/uuid%3Ad4085d73-4646-4e83-8e0b-c564facb7497?collection=education.

[14] F. Pisanò, R. Schipper, and G. J. Schreppers. “Input of fully 3D FE soil-structure modelling to the operational analysis of jack-up structures”. In: *Marine Structures* 63 (Jan. 2019), pp. 269–288. ISSN: 0951-8339. DOI: 10.1016/J.MARSTRUC.2018.09.011. URL: https://repository.tudelft.nl/islandora/object/uuid%3A949b2a91-b3ef-4836-8998-c560e5e884c2.

[15] S. Rajasekaran. “Free vibration of single-degree-of-freedom systems (under-damped) in relation to structural dynamics during earthquakes”. In: *Structural Dynamics of Earthquake Engineering* (2009), pp. 54–55. DOI: 10.1533/9781845695736.1.44.

[16] A. Savitzky and Marcel J. E. Golay. “Smoothing and Differentiation of Data by Simplified Least Squares Procedures.” In: *Analytical Chemistry* 36.8 (July 1964), pp. 1627–1639. DOI: 10.1021/ac60214a047.

[17] *scipy.stats.exponweib — SciPy v1.10.1 Manual*. 2. URL: https://docs.scipy.org/doc/scipy/reference/generated/scipy.stats.exponweib.html#scipy.stats.exponweib.

[18] Seajacks. *Siren*. URL: https://www.seajacks.com/self-propelled-jack-up-vessels/.

[19] C. E. S. de Souza and E. E. Bachynski-Polić. “Design, structural modeling, control, and performance of 20 MW spar floating wind turbines”. In: *Marine Structures* 84 (July 2022), p. 103182. ISSN: 0951-8339. DOI: 10.1016/J.MARSTRUC.2022.103182.

[20] X. Tian et al. “Experimental study on influencing factors of hydrodynamic coefficient for jack-up platform”. In: *Ocean Engineering* 193 (Dec. 2019). ISSN: 00298018. DOI: 10.1016/J.OCEANENG.2019.106588.

[21] *Time-series of surface elevations by individual waves for a certain sea state.* Apr. 2020. URL: http://www.coastalwiki.org/wiki/Statistical_description_of_wave_parameters.

[22] R. van der Valk. “Hoist and boom wire dynamics during offshore heavy lifting”. TU Delft, Sept. 2017. URL: https://repository.tudelft.nl/islandora/object/uuid:f347a0c0-98aa-45e7-881d-fee5ce5ab0f4?collection=education.

[23] J. H. Vazquez et al. *Jack up primer*. 2005.

[24] S. A. Velinsky. “General nonlinear theory for complex wire rope”. In: *International Journal of Mechanical Sciences* 27 (7-8 Jan. 1985), pp. 497–507. ISSN: 0020-7403. DOI: 10.1016/0020-7403(85)90040-2.

[25] Det Norske Veritas. *DNV-RP-C205 Environmental conditions and environmental loads*. DNV-RP-C205. Oslo, Norway: Det Norske Veritas, 2019.

[26] Det Norske Veritas. *STANDARD FOR CERTIFICATION No. 2.22 LIFTING APPLIANCES*. No. 2.22. Oslo, Norway: Det Norske Veritas, 2019.

[27] A. S. Verma et al. “Effects of Wind-Wave Misalignment on a Wind Turbine Blade Mating Process: Impact Velocities, Blade Root Damages and Structural SafetyAssessment”. In: *Journal of Marine Science and Application* 19 (2 June 2020), pp. 218–233. ISSN: 1671-9433. DOI: 10.1007/S11804-020-00141-7. URL: https://repository.tudelft.nl/islandora/object/uuid%3Abea0448a-c635-4ab7-8d6c-b13a06055541.

[28] A. S. Verma et al. “Response-based assessment of operational limits for mating blades on monopile-type offshore wind turbines”. In: *Energies* 12 (10 2019). ISSN: 19961073. DOI: 10.3390/EN12101867.

[29] Y. Zhao. *Numerical modeling and analysis of the dynamic motion response of an offshore wind turbine blade during installation by a jack-up crane vessel*. June 2019. DOI: 10.1016/J.OCEANENG.2018.07.049.

[30] Y. Zhao et al. “Numerical modeling and analysis of the dynamic motion response of an offshore wind turbine blade during installation by a jack-up crane vessel”. In: *Ocean Engineering* 165 (Oct. 2018), pp. 353–364. ISSN: 0029-8018. DOI: 10.1016/J.OCEANENG.2018.07.049.

A

Equation of the natural period of the various pendulum configurations

Below, the equations to calculate the natural period for each pendulum configuration, are shown. For configuration two and four, the equations have been derived using Lagrange.

Configuration one:

$$T := 2 \cdot \pi \cdot \mathrm{sqrt}\left(\frac{L}{g}\right) \tag{A.1}$$

Configuration two:

$$I \cdot \omega^4 \cdot \left(\left(l_1^2 + l_2^2\right) \cdot m + I\right) - g \cdot m \cdot \omega^2 \cdot (l_1 + l_2) \cdot (m \cdot l_1 \cdot l_2 + I) + g^2 \cdot l_1 \cdot l_2 \cdot m^2 = 0 \tag{A.2}$$

With:

$$I = \frac{1}{3} \cdot m_2 \cdot (L_{tower})^2 + m_2 \cdot \left(L_{sling}\right)^2 \tag{A.3}$$

Configuration three:

$$T := 2 \cdot \pi \cdot \mathrm{sqrt}\left(\frac{I}{g \cdot L}\right) \tag{A.4}$$

Configuration four:

$$\begin{aligned}(l_1^2 \cdot ((m_1 \cdot l_2^2 + I) \cdot m_2 + I \cdot m_1) + I \cdot \omega^4 \cdot (m_2 \cdot l_2^2 + I)) - g \cdot \omega^2 \cdot (l_2 \cdot m_2 \cdot l_1^2 \cdot (m_1 + m_2) + \\ l_1 \cdot (m_1 + m_2) \cdot (m_2 \cdot l_2^2 + I) + I \cdot l_2 \cdot m_2) + g^2 \cdot l_1 \cdot l_2 \cdot m_2 \cdot (m_1 + m_2) = 0\end{aligned} \tag{A.5}$$

With:

$$I = \frac{1}{3} \cdot m_2 \cdot (L_{tower})^2 + m_2 \cdot \left(L_{sling}\right)^2 \tag{A.6}$$

In the equation above the following parameters are used:

L	=	sling length when the hoist block is not modelled
l_1	=	sling length between crane tip and hoist block
l_2	=	distance between hoist block and centre of gravity of load in hook
m	=	total mass
m_1	=	mass of hoist block
m_2	=	mass of load in hook
g	=	gravity
ω	=	natural frequency

B

Input

B.1. Confidential

C

Maximum moment distribution

C.1. confidential

D

Results spectral analysis

D.1. Conditential

E

Probability of each sea-state

E.1. Conditential

F

Annual probability of failure

F.1. Conditential

G

Distributions for different exposure times

G.1. Conditential

H

Confidential Annex

CONFIDENTIAL

Figure H.1: Slewing angle of the crane

CONFIDENTIAL

Figure H.2: Luffing angle of the crane

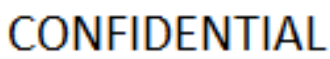

Figure H.3: Translated slewing angle of the crane

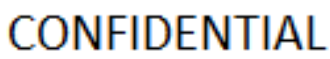

Figure H.4: Translated luffing angle of the crane

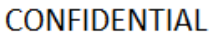

(a) Distribution of the installation time of the towers

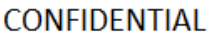

(b) Distribution of the installation time of the nacelles

Figure H.5: Distribution of the installation time of the tower and nacelle lifts

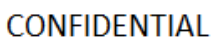

(a) Distribution of the installation time of the blades

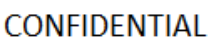

(b) Distribution of the time the yoke is in the hook

Figure H.6: Distribution of the installation time of the blade and yoke lifts

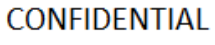

(a) Normalized PDF of the maximum moment for a 90% confidence interval

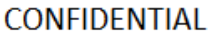

(b) Normalized PDF of the maximum moment for a 95% confidence interval

Figure H.7: Normalized PDF of the maximum moment for a 90% and 95% confidence interval

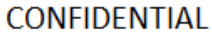

Figure H.8: Normalized PDF of the maximum moment for a 99% confidence interval

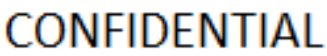

Figure H.9: Distribution of ratio β for the different T_p

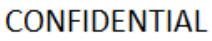

(a) zeroth-order moment of the spectrum for different T_p

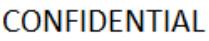

(b) T_z of the spectra for the different T_p

Figure H.10: zeroth-order moment and T_z of the spectrum for different T_p

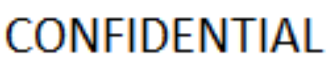

Figure H.11: Ratio β for different wave periods

Figure H.12: PDF of the distribution of the maximum moment for multiple seed sizes

(a) Example spectrum without filtering

(b) Example spectrum with filtering

Figure H.13: Difference caused by filtering using a Savitzky-Golay filter

Figure H.14: Influence of exposure time on the 90% confidence interval maximum moment

Figure H.15: Distribution of the maximum moment for a T_p of 3 seconds, for different exposure times

Figure H.16: Distribution of the maximum moment of each seed, with different types of fitted probability distributions

CONFIDENTIAL

Figure H.17: 90% confidence interval maximum moment and significant value for different T_p

CONFIDENTIAL

(a) Spectrum for a T_p of 3 seconds of a nacelle lift with a sling length of 170 meters

CONFIDENTIAL

(b) Spectrum for a T_p of 7 seconds of a nacelle lift with a sling length of 170 meters

Figure H.18: Spectra of a nacelle lift with a sling length of 170 meters

Table H.1: MCC for different side-lead angles

Side-lead angle [degree]	0.1	0.2	0.5

Table H.2: Exposure time of each lifting operation

Lifting operation	Tower	Nacelle	Blade	Yoke
Exposure time [min], confidence interval 90%	-	-	-	-